Monthly Notices
of the
ROYAL ASTRONOMICAL SOCIETY

MNRAS **453,** 1164–1185 (2015) doi:10.1093/mnras/stv1646

Properties of cosmological filaments extracted from Eulerian simulations

C. Gheller,[1⋆] F. Vazza,[2,3⋆] J. Favre[1] and M. Brüggen[2]

[1]*ETHZ-CSCS, Via Trevano CH-131, Lugano, Switzerland*
[2]*Hamburger Sternwarte, Gojenbergsweg 112, D-21029 Hamburg, Germany*
[3]*INAF-Istituto di Radio Astronomia, Via Gobetti I-101, Bologna, Italy*

Accepted 2015 July 17. Received 2015 July 17; in original form 2015 January 27

ABSTRACT

Using a new parallel algorithm implemented within the VisIt framework, we analysed large cosmological grid simulations to study the properties of baryons in filaments. The procedure allows us to build large catalogues with up to $\sim 3 \times 10^4$ filaments per simulated volume and to investigate the properties of cosmic filaments for very large volumes at high resolution (up to 300^3 Mpc^3 simulated with 2048^3 cells). We determined scaling relations for the mass, volume, length and temperature of filaments and compared them to those of galaxy clusters. The longest filaments have a total length of about 200 Mpc with a mass of several 10^{15} M$_\odot$. We also investigated the effects of different gas physics. Radiative cooling significantly modifies the thermal properties of the warm-hot-intergalactic medium of filaments, mainly by lowering their mean temperature via line cooling. On the other hand, powerful feedback from active galactic nuclei in surrounding haloes can heat up the gas in filaments. The impact of shock-accelerated cosmic rays from diffusive shock acceleration on filaments is small and the ratio between cosmic ray and gas pressure within filaments is of the order of ∼10–20 per cent.

Key words: methods: numerical – galaxies: clusters: general – intergalactic medium – large-scale structure of Universe.

1 INTRODUCTION

Simulations of structure formation predict that about 50 per cent of the baryons reside in a filamentary web of tenuous matter at temperatures of 10^5–10^7 K connecting already virialized structures (e.g. Cen & Ostriker 1999; Davé et al. 2001). This plasma is referred to as 'Warm-Hot Intergalactic Medium' (WHIM).

The total matter (mostly Dark Matter, DM) of the cosmic web is traced by galaxies that populate filamentary and wall-like structures, the largest of which have sizes in excess of 100 Mpc h^{-1} (e.g. Zeldovich, Einasto & Shandarin 1982; Einasto et al. 1984; Geller & Huchra 1989; Gott et al. 2005). A first glimpse of this cosmic web in the local Universe was offered by the first CfA redshift slice (e.g. de Lapparent, Geller & Huchra 1986). In recent years, this view has been expanded by the 2dFGRS (e.g. Ochsenbein, Bauer & Marcout 2000), Sloan Digital Sky Survey (SDSS; e.g. Tegmark et al. 2004) and *IRAS* (e.g. Courtois et al. 2013) galaxy redshift surveys.

A direct detection of the gas in the cosmic web is more challenging because the low densities and temperatures are unfavourable, and so far only very little evidence has been produced. Baryons in filaments may be revealed in the soft X-ray band but the few reported detections are still controversial (e.g. Finoguenov, Briel & Henry 2003; Werner et al. 2008; Nicastro et al. 2010, 2013). In the radio band, only very few possible detections have been reported (Bagchi et al. 2002; Kronberg et al. 2007; Giovannini et al. 2010; Farnsworth et al. 2013). These sources are more likely to be related to merger shocks than to the accretion shocks described by numerical simulation.

Recently, the Sunyaev–Zeldovich (SZ) effect has been used to probe filamentary gas connections between galaxy clusters, and a first indication for the detection of a filament between the cluster pair A399-A401 has been reported by Planck Collaboration VIII, et al. (2013). They observed a significant thermal SZ signal in the regions beyond the virial radii. A joint X-ray SZ analysis constrained the temperature of the filamentary region to $kT = 7.1 \pm 0.9$ keV and the baryon density to $3.7 \pm 0.2 \times 10^{-4}$cm^{-3}. However, this should represent only the dense and small-sized version of much larger (∼10–100 Mpc long) objects that the cosmic volume can contain.

The evolution of the cosmic web can be explained through the interaction of the initial pattern of density waves at different scales, with random and uncorrelated spatial phases. The main skeleton of the cosmic web is determined by the initial gravitational potential field (Einasto et al. 2011). Recently, Obreschkow et al. (2013) studied in detail the emergence of the filamentary structure of the cosmic web from the phase information embedded in the pattern of initial cosmological fluctuations. During their evolution initial fluctuations interact in a non-linear way, with the generation of non-random and correlated phases, which lead to the spatial pattern of the present cosmic web (Bond, Kofman & Pogosyan 1996).

⋆ E-mail: cgheller@cscs.ch (CG); franco.vazza@hs.uni-hamburg.de (FV)

The non-linear evolution can be described by *N*-body simulations that provide an accurate picture of the evolution of the gravitational potential and of the DM haloes.

With the growing capabilities of *N*-body cosmological simulations, increasing effort has been devoted to the implementation of reliable methodologies for the identification of complex structures in the matter distribution, aiming at the accurate segmentation of the cosmic web into clusters, filaments, walls and voids (e.g. Cautun et al. 2014, and references therein for a recent review). The list of attempted methods is too long to enable a complete summary here. The algorithms can be broadly grouped into: (a) geometrical and tessellation methods, based on the topological analysis of the density field by means of sophisticated mathematical approaches (e.g. Stoica et al. 2005; Sousbie et al. 2008; Aragón-Calvo, van de Weygaert & Jones 2010; González & Padilla 2010; Bleuler et al. 2015; Chen et al. 2015), (b) morphological methods, that classify the 3D distribution of matter based on the density Hessian and/or the tidal or velocity shear fields (e.g. Aragón-Calvo et al. 2007; Hahn et al. 2007; Cautun et al. 2014). Recently, Cautun et al. (2014) compared the results of different filament detection methods with the *NEXUS* algorithm, which is an advanced multiscale analysis tool to identify the different morphologies of cosmic structures, based on the analysis of density, tidal field, velocity divergence and velocity shear as tracers of the Cosmic Web. They concluded that most methods agree on the largest filaments, but parameters such as the diameter of filaments depend on the resolution and the method. Most of the differences are found in the most rarefied environments, where density contrasts are very small and methods working on shears or local differences are less sensitive. As a result, different algorithms agree well on the total mass in filaments (∼90 per cent of the total mass is captured in all methods) and worse on the total volume (only a ∼60 per cent of the volume is equally identified).

So far, the study of the properties of the baryons in the low-density components of the cosmic web (such as in filaments) have been investigated less systematically. Low-density environments outside of galaxy clusters have been studied with cosmological hydrodynamical simulations (e.g. Davé et al. 2001; Viel et al. 2005; Dolag et al. 2006; Dolag, Bykov & Diaferio 2008, and references therein). The effect of energy feedback from galactic activity on the observable properties of the WHIM has been analysed by, for example, Cen & Ostriker (2006), Roncarelli et al. (2006), Hallman et al. (2007), Kang et al. (2007), Roncarelli et al. (2012), Bolton et al. (2014), Vogelsberger et al. (2014). Hydrodynamical simulations suggest that regions of moderate overdensity such as filaments host a significant fraction of the WHIM (e.g. Cen & Ostriker 1999; Davé et al. 2001), and they are surrounded by strong stationary accretion shocks, where the cosmic gas is first shock heated to temperatures $\geq 10^4$ K (e.g. Miniati et al. 2000; Ryu et al. 2003; Pfrommer et al. 2006). Using a more idealized setup, Klar & Mücket (2012) simulated the impact of different physical processes as well as of the scale dependencies in the formation of ∼5 Mpc filaments starting from a single-scale perturbation. The simulated filaments exhibit an isothermal core, whose temperature is balanced by radiative cooling and heating due to the UV background, yielding a multiphase medium. The WHIM is also expected to host supersonic turbulent motions (Iapichino et al. 2011; Vazza et al. 2014b), and the decay of such motions can cause the amplification of weak primordial magnetic fields up to the ∼nG level (Ryu et al. 2008a; Vazza et al. 2014b).

In this work, we combined state-of-the-art cosmological hydrodynamic simulations performed using the ENZO code (Section 2) with a novel methodology for the identification of the cosmic web, based on the gas matter distribution. The gas distribution can be accurately described by ENZO's Eulerian hydrodynamic solver irrespectively of the mass density. Using the gas mass density, we have developed an *Isovolume* based technique to identify the cosmic web structures. Isovolumes represent a class of algorithms that tackle the problem of separating regions of space with distinct physical properties, in our case with density above and below a given threshold. We tuned the selection in gas overdensity specifically to extract the mass distribution associated with the filamentary structure of the cosmic web. However, the same approach can also be used to identify other structures, such as voids, sheets and haloes.

The resulting methodology is described in detail in Section 3. The corresponding performance and scaling properties on high-performance computing systems are presented in Appendix A together with a discussion on the influence on the results of the parameters characterizing our approach.

The methodology is simpler than the aforementioned methods while avoiding the drawbacks of algorithms that rely on DM particles. In regions where the matter density is comparable to the mean cosmic density, as in the WHIM, the numerical noise arising from the graininess of the DM particles distribution can affect the estimates of the properties of the cosmic web. Further advantages of using the gas component are that it is immediately related to observations, and that the effect of additional physical processes (e.g. cooling and feedback from galactic activity) influencing the gas properties can be studied in detail. Using the gas component as a tracer of the gravitational potential, the method is insensitive to cosmic shear fields and to the local dynamics of DM.

We have analysed the statistical and thermodynamic properties of filaments identified through our procedure, and investigated their dependence on the spatial resolution and the assumed physics, in particular the cooling and heating processes. The results are presented in Sections 3.3 and 4 and discussed in Section 5. Our finally summary is given in Section 6 where we discuss possible future numerical developments that will allow a more quantitative prediction of the observable properties of the WHIM through the inclusion of mechanisms such as chemical enrichment, metal-dependent cooling and magnetic fields.

2 SIMULATIONS

Our simulations are run with a customized version of the grid code ENZO (Bryan et al. 2014), presented in Vazza, Gheller & Brüggen (2014a). ENZO is a parallel code for cosmological (magneto-)hydrodynamics, which uses a particle-mesh *N*-body method (PM) to follow the dynamics of the DM and (in this case) the Piecewise Parabolic Method (PPM; Colella & Woodward 1984) to evolve the gas component. On the basis of the public version of ENZO, we have implemented specific methods to describe the evolution and feedback of cosmic ray (CR) particles (Vazza et al. 2012), as well as our implementation of energy release from active galactic nuclei (AGN; Vazza, Brüggen & Gheller 2013) and supernovae. The suite of simulations analysed in this work has been designed to study the properties of CRs, the acceleration of relativistic hadrons at shocks and their energy feedback on the baryon gas (Vazza et al. 2014a).

The simulations presented in this paper have been run with two flavours of CR-injection, based on a high-efficiency model by Kang & Jones (2007) (model '0') and on a lower efficiency model by Kang & Ryu (2013) (model '1').

Radiative cooling ('c' in the name descriptor of Table 1) has been modelled assuming a primordial composition of a fully ionized H–He plasma with a uniform metallicity of $Z = 0.3\,Z_{\odot}$ (where $Z_{\odot}$

Table 1. List of the simulations run for this project. Column 1: box size. Column 2: number of grid cells. Column 3: spatial resolution. Column 4: physical implementation. Column 5: identification name of each run. The ID must be read as follows: the first number refers to the box size, 1 referring to 216 Mpc h^{-1}, 2 to 108 Mpc h^{-1}, 3 to 54 Mpc h^{-1}. The second symbol refers to the physical model. Finally, the third number indicates the 1D computational mesh size in cells. These IDs will be adopted throughout the paper.

$L_{\rm box}$ [Mpc h^{-1}]	$N_{\rm grid}$	Δx[kpc h^{-1}]	Physics	ID
216	2048^3	105	Non-rad.+CR(KR13)	1-1_2048
216	1024^3	210	Non-rad.+CR(KR13)	1-1_1024
216	1024^3	210	Non-rad.+CR(KJ07)	1-0_1024
108	1024^3	105	Non-rad.+CR(KR13)	2-1_1024
108	1024^3	105	Non-rad.+CR(KJ07)	2-0_1024
108	1024^3	105	Cool1.+AGN feedback+CR(KR13)	2-c1_1024
108	1024^3	105	Cool2.+AGN feedback+CR(KR13)	2-c2_1024
54	1024^3	52	Non-rad.+CR(KR13)	3-1_1024
54	1024^3	52	Non-rad.+CR(KJ07)	3-0_1024
54	1024^3	52	Cool1.+AGN feedback+CR(KR13)	3-c1_1024
54	512^3	105	Non-rad.+CR(KR13)	3-1_512
54	512^3	105	Non-rad.+CR(KJ07)	3-0_512
54	512^3	105	Cool1.+AGN feedback+CR(KR13)+AGN	3-c2_512
54	256^3	210	Non-rad.+CR(KR13)	3-1_256

is the solar metallicity), using the Astrophysical Plasma Emission Code (APEC) emission model (e.g. Smith et al. 2001). For the cold gas, with temperature $T \leq 10^4$ K, we use the cooling curve of Smith et al. (2011), which is derived from a complete set of metals (up to an atomic number 30), obtained with the chemical network of the photo-ionization software CLOUDY (Ferland et al. 1998). In order to model the UV re-ionization background (Haardt & Madau 1996), we enforced a temperature floor for the gas in the redshift range $4 \leq z \leq 7$, as discussed in Vazza et al. (2010).

All radiative simulations presented here also include the effect of feedback from AGN, which are placed in high-density peaks ($n \geq n_{\rm AGN} = 10^{-2}$ cm^{-3}). This method by-passes, both, the problem of monitoring the mass accretion rate on to the central black hole within each galaxy, and the complex small-scale physical processes which couple the energy from the black hole to the surrounding gas (i.e. the launching of strong winds due to the radiation pressure of photons from the accretion disc). This is unavoidable, given that our best resolution is orders of magnitudes larger than the accretion disc region, let alone the difficulty of modelling the radiative transfer of photons from the accretion region. At each feedback event we add an energy of $E_{\rm AGN} \sim 10^{59}$ erg during a single time-step, which typically raises the temperature in the cell to $\sim 5 \times 10^7$–5×10^8 K at the injection burst. We model the feedback as a 'bipolar thermal outflow', i.e. the thermal energy is released into the ICM along two cells on opposite sides of the AGN cell, and the direction of the two jets is randomly selected along one of the three coordinate axes of the simulation. In the runs analysed for this work we include two slightly different implementations of AGN feedback in simulations with radiative cooling, which produce rather different cluster scaling relations at $z = 0$. In the first run ('c1'), we trigger thermal feedback whenever the local maximum density exceeds the (comoving) gas density threshold, $n_{\rm AGN}$, starting from $z = 1$. In the second run, the AGN feedback is started at $z \leq 4$ (run 'c2'). While the first approach is found to quench the radiative cooling inside most of haloes but fails to produce cluster scaling relations that match observations (i.e. the M–T and $L_{\rm X}$–T relations are much flatter than observations), the second produces a tilt in scaling relations that agree well with observations, and is thus our preferred AGN-feedback method.

At all redshifts the heating by the reionizing background largely exceeds the heating contribution from CRs, which lose energy via interactions with thermal particles of the ICM (Guo & Oh 2008). This energy exchange is modelled at run-time in our method for CRs, but it becomes important only for high gas densities [$\rho/(\mu m_{\rm p}) > 10^{-2}$ cm^{-3}] that are typical of galactic cool cores (Vazza et al. 2014a).

The runs analysed here assume a *Wilkinson Microwave Anisotropy Probe* 7-year cosmology with $\Omega_0 = 1.0$, $\Omega_{\rm B} = 0.0455$, $\Omega_{\rm DM} = 0.2265$, $\Omega_\Lambda = 0.728$, Hubble parameter $h = 0.702$, a normalization for the primordial density power spectrum $\sigma_8 = 0.81$ and a spectral index of $n_{\rm s} = 0.961$ for the primordial spectrum of initial matter fluctuations, starting the runs at $z_{\rm in} = 30$ (Komatsu et al. 2011).

Table 1 lists the simulations used for this work, showing the different choices for the physical mechanisms, as well as the grid size. We simulated three independent cosmological volumes with boxes of sides 216 Mpc h^{-1}, 108 Mpc h^{-1} and 54 Mpc h^{-1}, respectively. In order to monitor resolution effects for each case, we produced re-simulations of each of these with a different number of cells (from 2048^3 to 256^3) and DM particles. In general, the missing effects of non-gravitational physics, such as radiative gas cooling and AGN feedback, are much more evident at high resolutions, where gas density and hence radiative losses are higher. For this reason, our study of the impact of non-gravitational physics is based largely on the smallest box (with side 54 Mpc h^{-1}). On the other hand, the impact of different CR injection efficiencies on the outer cluster profiles is also captured at a lower spatial resolution, and therefore all our boxes include a study using different acceleration recipes.

3 IDENTIFICATION OF FILAMENTS

Our procedure to identify filaments uses the gas mass density to separate over- from under-dense regions. With this criterion, a single physical parameter determines the identification procedure, with no further arbitrary settings of other physical quantities. The selection is further refined by considering the numerical resolution of the simulations and the expected geometry of a filament. These

additional criteria mainly affect small objects (of typical size less than 1 Mpc^3). The resulting methodology is implemented based on a combination of different algorithms developed and optimized in the context of material interface reconstruction. The accurate identification of the interface between two or more materials represents a major issue in these applications since a single computational cell can be composed of pieces of different materials. Various solutions have been developed in order to reconstruct interfaces, both for simulations and for visualization and data analysis. Examples are provided by Meredith & Childs (2010), Fujishiro, Maeda & Sato (1995), Harrison, Childs & Gaither (2011), Anderson et al. (2010) and references therein.

We can identify two distinct material phases: the warm/hot gas which fills collapsed cosmological structures on one side, and the cold under-dense phase typical of voids on the other side. The accurate representation of the boundaries between these two phases is the key to define the properties of the identified objects. In this work, we have adopted an *Isovolume*-based approach, described in Meredith (2004). A quantitative evaluation of this approach and of its performance, compared to other methodologies, can be found in Meredith & Childs (2010). It has been further evaluated for our specific needs. The resulting accuracy and performance are presented in Section 3.2 and Appendix A, respectively.

In order to implement a computationally efficient, flexible and extensible filament reconstruction procedure, we have exploited the VisIt data visualization and analysis framework (Childs et al. 2012). VisIt is designed for the efficient processing of large data sets through a combination of optimized algorithms, the exploitation of high-performance computing architectures, in particular through parallel processing, based on the MPI standard, and the support of client-server capabilities, allowing efficient remote visualization. It can be used interactively, through a graphical user interface, and it can be scripted using the Python programming language in order to automate the data processing. Finally, it natively supports a number of file format adopted by popular astrophysical simulation codes, such as COSMOS, FLASH, GADGET, CHOMBO (besides, of course, ENZO) and in general all files adopting the VTK format.[1] We refer to the official documentation[2] for all the technical details on the software.

VisIt includes the aforementioned Isovolume algorithm, which, combined with the *Connected Components* filter (also provided by the software, Harrison et al. 2011), allows the segmentation of the data into distinct objects. An example of a filament identified and reconstructed by our procedure is shown by Fig. 1.

3.1 Filament identification procedure

The main steps performed by our implemented identification procedure can be summarized as follows.

(i) *Identification of large clumps.* In a first step we separate filaments from galaxy clusters. Clusters can be described as high-density clumps in the matter distribution. Such clumps can be identified first by selecting isovolumes with

$$\frac{\varrho_{\mathrm{BM}}}{\varrho_0} \geq a_{\mathrm{cl}}, \tag{1}$$

where ϱ_{BM} is the cell's baryon mass density, a_{cl} is a proper threshold and ϱ_0 is the critical density at present time. For each clump, VisIt returns the volume V_{cl} and the coordinates of its centre. At this point, assuming spherical symmetry, we calculate the radius of each cluster as:

$$R = \beta \left(\frac{3V_{\mathrm{cl}}}{4\pi} \right)^{1/3}, \tag{2}$$

where β is a multiplicative factor needed to rescale the radius to values of the order of 1 Mpc (expected for galaxy clusters). Setting $a_{\mathrm{cl}} = 100$ and $\beta = 10$ proved to be effective for a proper cluster characterization.

Clusters with radius $R \geq 1$ Mpc are discarded by removing all cells falling within spheres with centre in the cluster centroid and radius R.

(ii) *Filament identification.* The Isovolume algorithm is used once more on the residual cells to identify the volumes that obey equation (1), only with a new threshold a_{fil}. The exact results of the identification procedure depends critically on this parameter, whose setting will be discussed in Section 3.3 and Appendix A. The connected components algorithm is then used to combine cells belonging to distinct (i.e. non intersecting) filaments, assigning to each filament an Id (an integer number) and marking each cell belonging to a filament with that Id. For each filament, the volume (V_{fil}), the mass (M_{fil}) and the average temperature (T_{fil}) are calculated.

(iii) *Small clumps removal.* The next step consists of removing small objects with volumes $V_{\mathrm{fil}} < V_{\mathrm{res}}$. In order to have a unique volume cutoff for all simulations, the parameter V_{res} is set equal to the lowest spatial resolution of our runs, $V_{\mathrm{res}} = (0.3\ \mathrm{Mpc})^3$. This ensures that a filament is always larger than a single cell.

(iv) *Shape selection.* Although the previous steps are designed to eliminate small clumps and large galaxy clusters, nonetheless a few outsiders can still be present at this stage. Hence, we use the following two-stage cleaning procedure to remove all remaining round-shaped, isolated structures. First, we calculate the bounding box enclosing each identified object and accept as filaments all those objects with:

$$\mathrm{MAX}(r_{xy}, r_{xz}, r_{yz}) > \alpha, \tag{3}$$

where r_{ab} is the ratio between axes a and b of the bounding box. A value of $\alpha = 2$ ensures that the selected object stretches in a specific direction without being too restrictive. The second stage is intended to recover all those objects which do not match criterion purely based on axis ratio. This happens, for instance, to filaments lying along the bounding box diagonal. The second shape selection consists of calculating the filling factor F_V of each remaining object, defined as:

$$F_V = \frac{V_{\mathrm{fil}}}{V_{\mathrm{box}}}, \tag{4}$$

where V_{box} is the bounding box volume. All objects with $F_V < \varphi$ are classified as filaments. The value of φ is set according to the ratio between the volume of a cubic bounding box and that of a cylindrical filament lying on its diagonal, with a base radius set as a fraction, namely 1/5, of the box side. The values of the parameters α and φ are discussed in Appendix A.

(v) *Data export.* The properties of the cells belonging to each filament, such as the mass density, temperature, velocity, geometric and topological information, are exported to output files using the VTK format.[3] Since the number of cells identified as filaments is some

[1] http://www.visitusers.org/index.php?title=Detailed_list_of_file_formats_VisIt_supports

[2] https://wci.llnl.gov/codes/visit/manuals.html

[3] http://www.vtk.org/VTK/img/file-formats.pdf

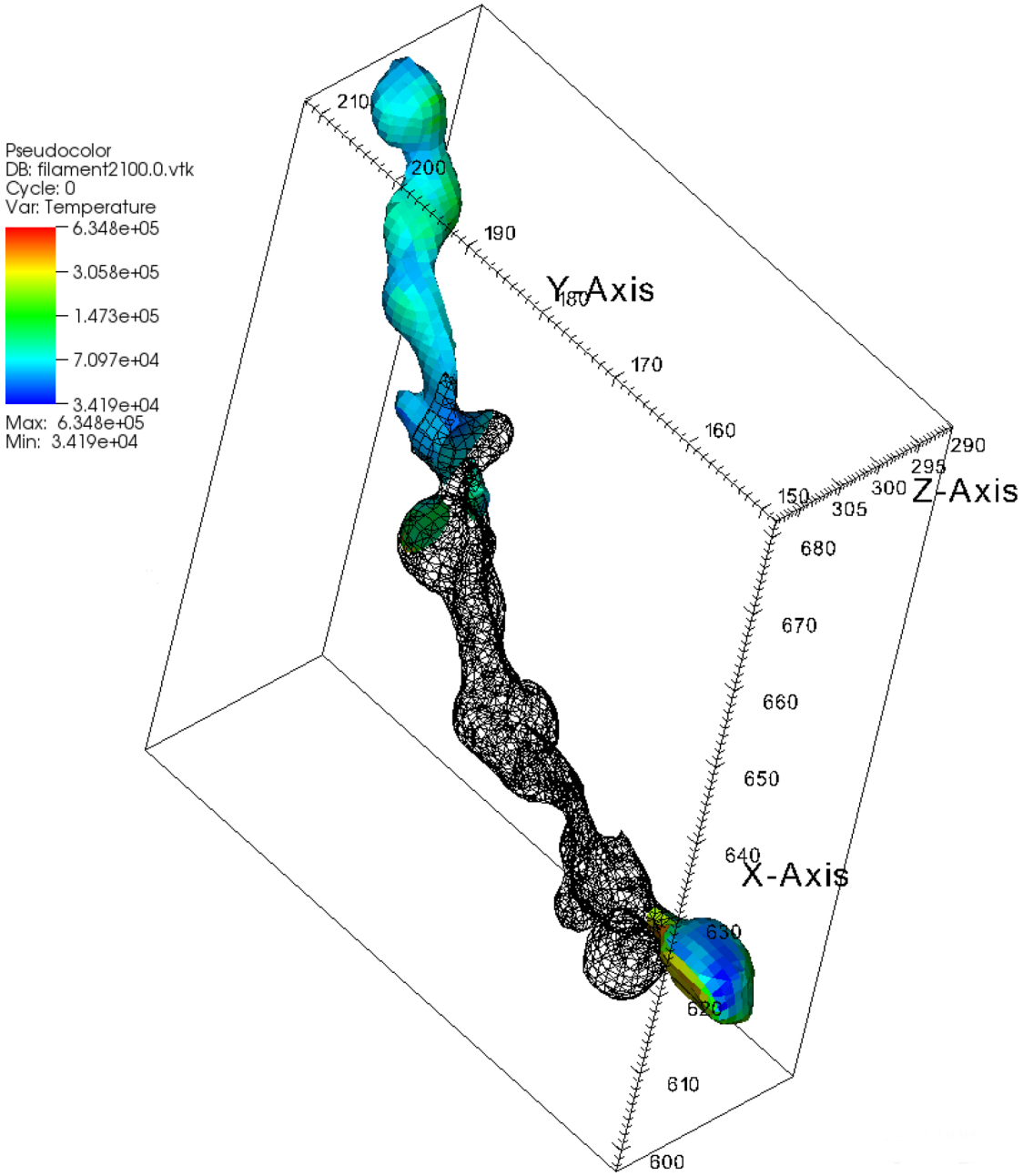

Figure 1. Example of a filament identified by the Isovolume method. Part of the object is outlined by the reconstructed surface mesh. The rest of the object is coloured with the temperature.

fraction of the total computational mesh, the file size is reduced correspondingly, making further data management and processing significantly easier and faster, which is very convenient for the large runs we use in this work.

3.2 Validation

We validate the Isovolume algorithm using spherically symmetric mass distributions modelled by Gaussian functions, representing idealized clusters and clumps, and cylindrical shapes to mimic filaments. For the filaments, the mass distribution orthogonal to the main axis is again modelled as Gaussian. We have first evaluated the accuracy of surface areas, volumes and density estimates as a function of the mesh resolution for single objects. Table 2 shows the error, calculated as the fractional difference between the calculated and the exact value of each of the three quantities, as a function of the radius, expressed in computational cells. For both spheres and cylinders, the density estimate is always accurate to $\leq$1 per cent. Volumes and surface areas are more sensitive to the resolution (see also Meredith & Childs 2010). For radii smaller than four cells, the error approaches (or is even larger, as in the case of the sphere's area) 10 per cent.

Data sets with various combinations of spheres and cylinders have been used to model the matter distribution from a

Table 2. Fractional error in the calculation of surface areas (Columns 2 and 5), volumes (Columns 3 and 6) and densities (Columns 4 and 7) for spheres and cylinders as a function of the distance (in cells) from the centre/axis (Column 1) of the sphere/cylinder.

R	$\delta A/A$ Sphere	$\delta V/V$	$\delta\varrho/\varrho$	$\delta A/A$ Cylinder	$\delta V/V$	$\delta\varrho/\varrho$
3.84	0.0762	0.1203	0.0024	0.0616	0.0836	0.0010
6.40	0.0265	0.0421	0.0011	0.0423	0.0453	0.0007
12.80	0.0049	0.0079	0.0002	0.0306	0.0183	0.0010
25.60	0.0003	0.0004	0.0002	0.0200	0.0048	0.0069
38.40	0.0014	0.0020	0.0021	0.0067	0.0207	0.0193

cosmological simulation. For all tests, a computational mesh of 128^3 cells is used. An example is presented in Fig. 2, where isovolumes at $a_{\rm fil} = 1$ and $a_{\rm fil} = 50$ are shown in the left and right panels, respectively. The accuracies of the volume and density estimates have been calculated as a function of $a_{\rm fil}$, obtaining the results presented in Table 3. Volume and density estimates are compared to those obtained by a simple algorithm which sums the contributions of all the cells above the given threshold, run at much higher resolution (1024^3). In all tests, the number of identified objects at each density threshold is correct. Only objects crossing the faces of the periodic computational box could not be counted properly because our procedure does not yet support periodic boundary conditions. In this case, a single object is split into multiple components, each treated as a separate filament. This leads also to underestimate the length of any filament crossing one of the box's side, as well as to the artificial increase of small-scale objects because of this artificial fragmentation. However, this problem is statistically not very relevant, as our volumes are typically much larger than the largest objects in the volume.

Table 3. Fractional error in the calculation of volumes (Column 2) and densities (Column 3) for combination of spheres and cylinders as a function of $a_{\rm fil}$ (Column 1).

$a_{\rm fil}$	$\delta V/V$	$\delta\varrho/\varrho$
0.25	0.026	0.010
0.50	0.025	0.011
0.75	0.024	0.012
1.0	0.023	0.013
2.0	0.020	0.018
5.0	0.016	0.022
50.0	0.047	0.004

The differences in the volume estimates are between 1.6 and 4.7 per cent. The maximum difference is at the highest density thresholds where the size of the various objects approaches the mesh resolution. The minimum is for $a_{\rm fil} = 5.0$ with objects that are still extended and have a simple geometry (disjoint spheres or cylinders). Density estimates show differences of the order of or less than 2 per cent.

3.3 Density threshold and spatial resolution

The parameter $a_{\rm fil}$ is critical for the characterization of the filament distribution. Its value is discussed below with additional considerations presented in Section 4.3 and in Appendix A. This parameter determines, together with the numerical spatial distribution, the features and the connectivity of the detected structures. Fig. 3 shows the mass distribution obtained using four different values of $a_{\rm fil}$, ranging from 0.5 to 2 for the model 2-1_1024, keeping all else constant. Similar results are obtained for the other models (not shown).

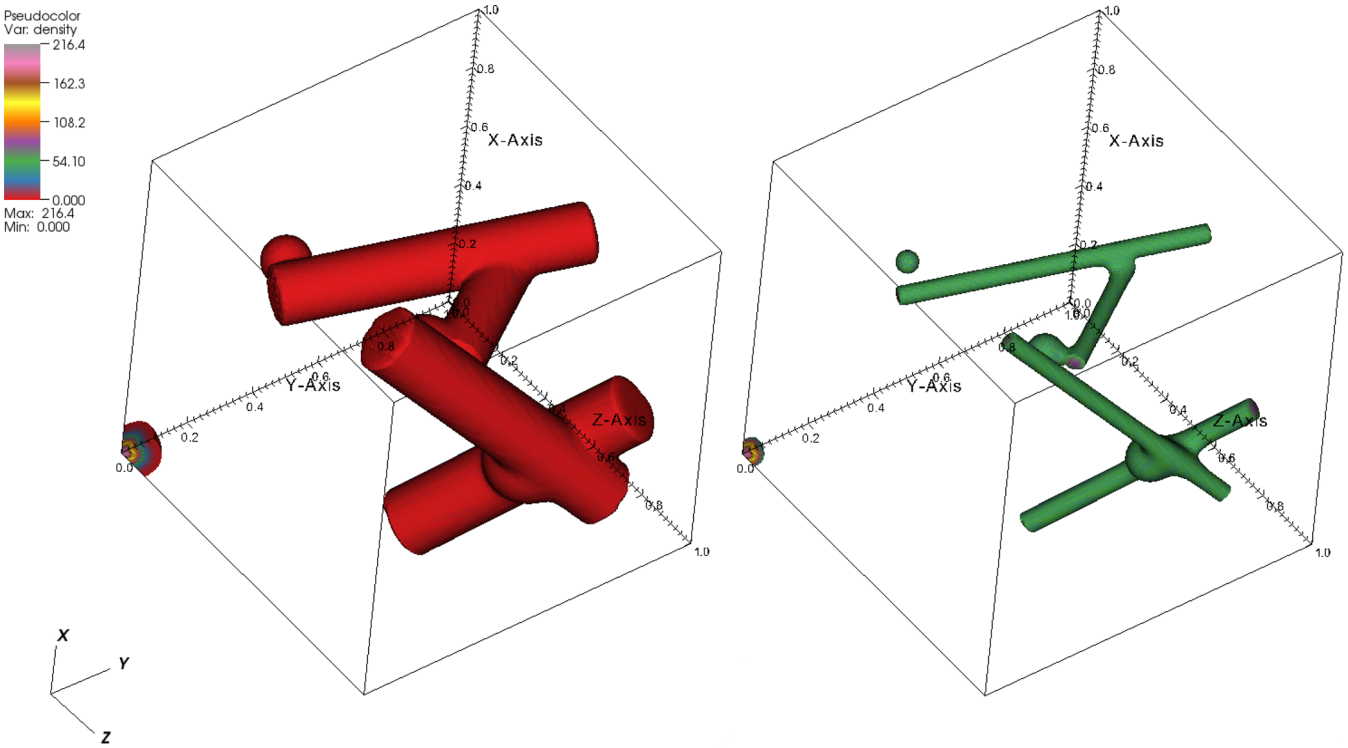

Figure 2. Isovolumes at $a_{\rm fil} = 1$ (left) and $a_{\rm fil} = 50$ (right) extracted from a test data set combining spheres and cylinders with different mass distribution.

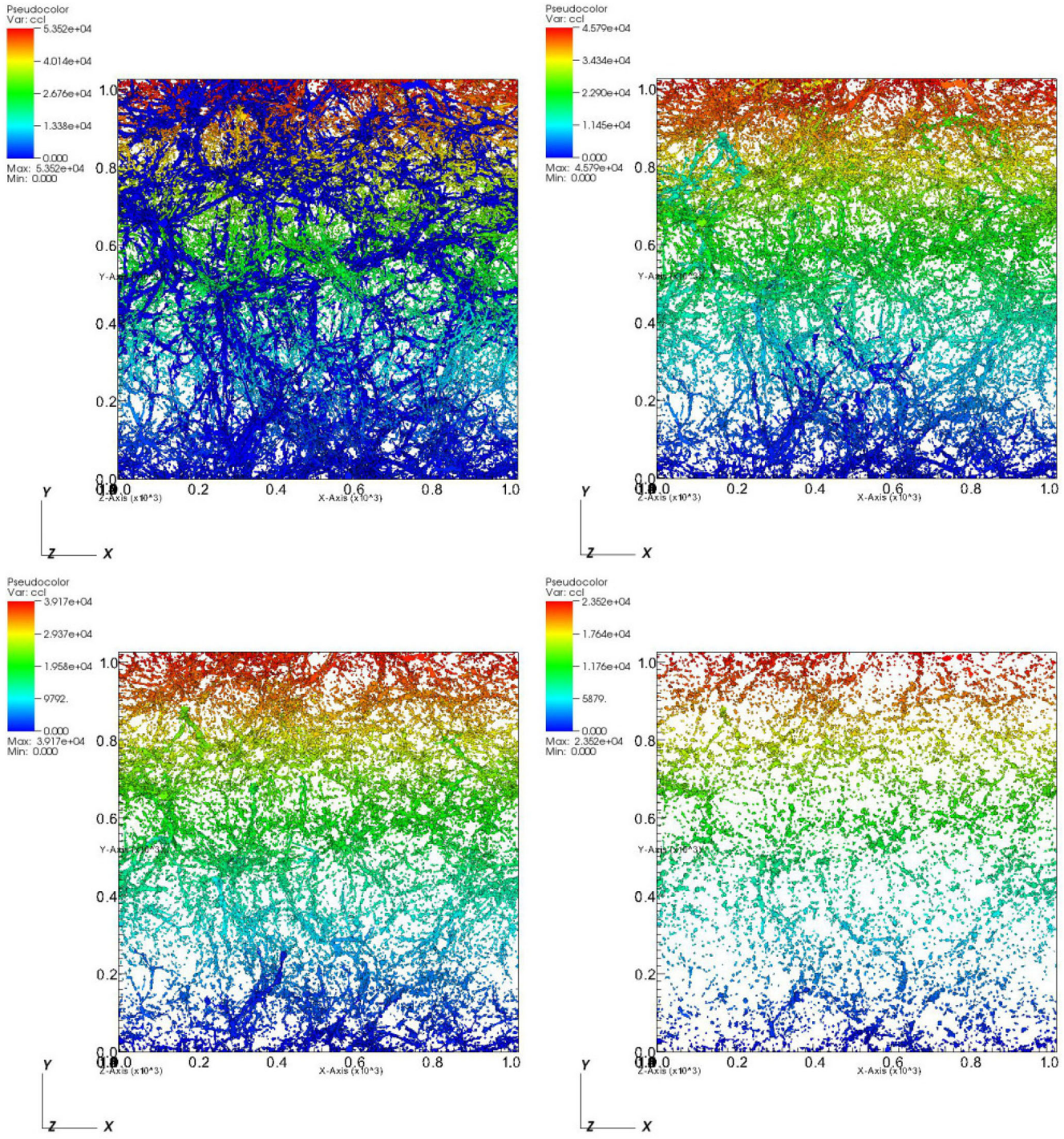

Figure 3. Mass distribution obtained using $a_{\rm fil} = 0.5$ (top left panel), 0.75 (top right), 1.0 (bottom left) and 2.0 (bottom right), for the model 2-1_1024. Each different object identified by our algorithm has a different colour.

Values of the mass density within this range are those expected for filaments (see e.g. Cen & Ostriker 1999; Davé et al. 2001).

A qualitative visual inspection of the distributions suggests the adoption of a value of $a_{\rm fil}$ in the range 0.75–1.0, smaller values leading to structures percolated across the whole computational box, and higher values generating clumpy distributions with limited (or even no) connectivity.

Fig. 4 shows the number of objects extracted from the simulations with box size of $(50{\rm Mpc}\,h^{-1})^3$ as a function of $a_{\rm fil}$. Results obtained with computational meshes of 1024^3, 512^3 and 256^3 cells are presented in order to investigate also the impact of spatial resolution on the results. Spatial resolution directly affects the number of objects identified by our algorithm, the differences decreasing at large values of the threshold parameter $a_{\rm fil}$. The number of filaments

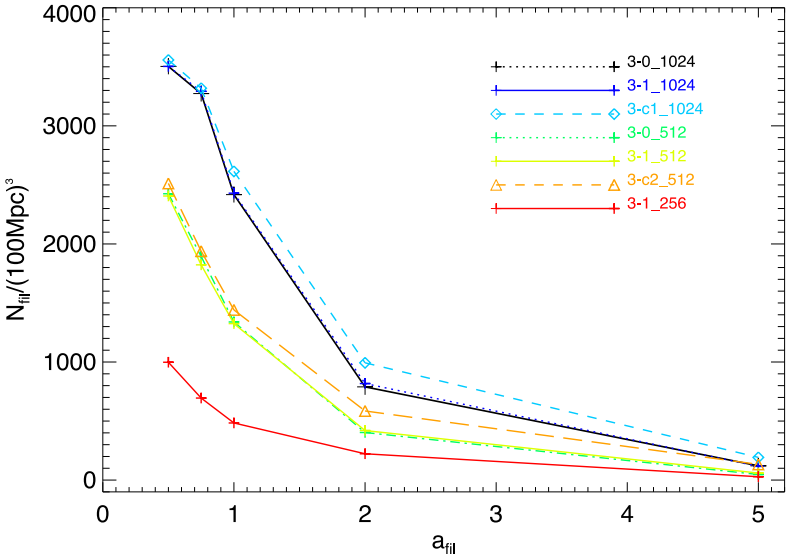

Figure 4. Number of filaments per 100 cubic Mpc as a function of $a_{\rm fil}$.

increases by a factor of ∼3.5 for $a_{\rm fil} = 0.5$ going from the 256^3 to the 1024^3 run, while the increase is only by a factor ∼2 for the largest threshold, $a_{\rm fil} = 5$. This shows that resolution strongly affects the identification of low-density filamentary structures below a given spatial scale, identifiable at about 0.2 Mpc, due to the larger diffusion of the gas at that resolution, which smoothens the mass density in the outer parts of the filaments, connecting structures otherwise distinct and leading to an overall decrease in the number of detected objects. As a consequence, among our data sets (Table 1), we expect the resolution to affect mainly the coarsest runs, with spatial resolution of 210 kpc h^{-1} (1-0_1024, 1-1_1024 and 3-1_256).

It is worth noting that for values of $a_{\rm fil}$ between 0.5 and 1, the various physical processes acting in the different simulations have the smallest influence on the statistics. Furthermore, at the highest resolution (1024^3 cells) the value $a_{\rm fil} = 1$ represents an inflection point for all the runs, suggesting a change in the properties of the distributions under investigation.

Fig. 5 (left panel) shows the dependence of the average mass density of a filament, $\varrho_{\rm avg}$, on the parameter $a_{\rm fil}$. As expected, the quantity $\varrho_{\rm avg}$ grows with increasing $a_{\rm fil}$ since lower-density regions are progressively cut out. The growth is almost linear and the slope higher for the 'c1' model, due to the cooling processes which dominate the AGN feedback. In model 'c2', that has effective AGN feedback, the effect of cooling is completely compensated by the energy injection, which raises the pressure and stops the infall of matter. The runs with CRs, '0' and '1', give similar results at all resolutions. This indicates that CRs only have a small effect on the dynamics of the gas within filaments. The model 'c1' has densities higher than the other models, due to the much lower thermal support within the collapsing structures, leading to highly compressed matter distributions. The trend with resolution of the mean gas density shows that for most of the investigated threshold values $a_{\rm fil}$ (with the exception of $a_{\rm fil} > 4$ extractions, which should be dominated by low-number statistics) the mean density increases with resolution, due to the higher achievable compression and the increased presence of substructures within filaments.

The right panel of Fig. 5 shows the average temperature of gas in filaments, $T_{\rm avg}$, as a function of $a_{\rm fil}$. Also the temperature increases with the density threshold parameter, faster for $a_{\rm fil} < 1.0$. At higher values, the temperature grows slowly with density. Inner parts of the filaments are thermalized at an almost constant temperature by shock waves propagating from the centre outwards. The outer part of the filaments, captured only at low $a_{\rm fil}$, can comprise non-shocked cells that lower the average temperature. The most striking feature of the graph is the trend of temperature with resolution. The lowest resolution run (256^3) presents the largest average temperature, at all investigated $a_{\rm fil}$, and further increase in resolution is followed by a decreased mean temperature. This trend is caused by the weakening of outer accretion shocks (yielding a lower thermalization efficiency in filaments) when resolution is increased, an effect already mentioned in Vazza et al. (2014a). On the opposite end, the model 3-c1_1024 has the lowest average temperatures at all values of $\varrho_{\rm avg}$, as a result of the strong effect of cooling. The 'c2' model has a peculiar behaviour. At low densities, cooling tends to dominate AGN feedback and the resulting average temperatures are clearly below all the other models (all but 'c1'). However, when higher-density objects are selected, AGN heating dominates, leading to the highest temperatures (neglecting the 256^3 case). The analysis of these results indicates that overall a value $a_{\rm fil} = 1$ is a suitable choice to identify filamentary structures. This choice of parameter is further supported by the analysis of the density and mass profiles discussed in Section 4.3. Hence, this will be the fiducial value for the rest of the paper.

4 PROPERTIES OF THE FILAMENTS

By keeping our fiducial density threshold of $a_{\rm fil} = 1.0$ we identified all filaments in the simulated data sets and computed their average properties, as a function of resolution and of the adopted physics. About 30 000 filaments were identified in our largest run (1-1_2048) and about 1000 objects in our highest resolution runs.

4.1 Visual analysis

In Fig. 6, we show eight objects extracted from one of our highest resolution runs (3-1_1024), as a representative sample of the filaments identified by our procedure. The eight objects are between 10 and 28 Mpc long, the longest being that with ID=7887 (27.9 Mpc).

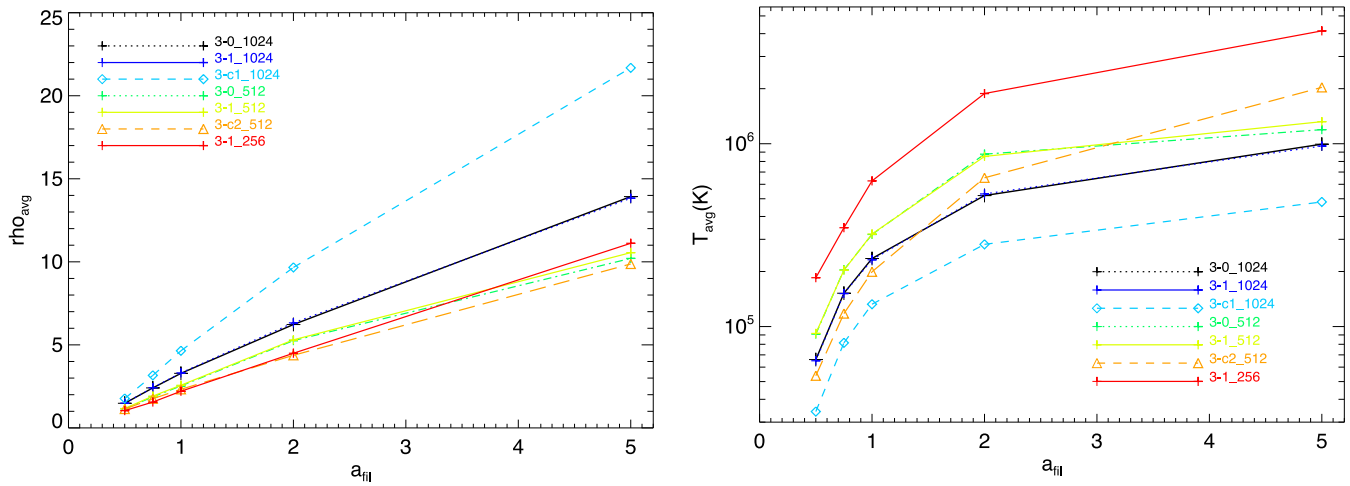

Figure 5. Average baryonic mass density (left panel) and temperature (right panel) in filaments as a function of $a_{\rm fil}$.

In the top left panel the selected filaments are presented together in order to show their location and to compare them to each other. The other panels are close-ups on each single object. Colours represent the temperature of the density isovolumes. The images show how filaments can have heterogeneous geometries, depending on the environment in which they lie. In some cases, as for filaments 678, 6397, and 2957, they have elongated and rather regular shapes, with comparable thickness and surface temperature. They have one or two main blob-like structures and they typically bridge pairs of massive galaxy clusters. We indicate such structures as 'giant bridges'. On the other hand, filaments 7887, 3153 and 14599 have a more branchy structure, with multiple blob-like components and very thin segments, which present a systematically colder surface, and several branches. Another peculiar type of filament is represented by filament 2131, which is more than 16 Mpc long and is much thinner and colder than all the other objects. The nature of these objects requires specific investigation to be fully understood. However, their features point towards filaments in an early evolutionary stage, with ongoing mass accretion heated up by a first generation of weak shocks propagating in a rather under-dense environment, and a total enclosed over-density which is just above our detection threshold. This class of filaments can be called 'long-thin'. Finally, as in the case of filament 8975, we find objects for which it is difficult to recognize the typical characteristics expected for filaments. They are found in rich regions and connect multiple larger haloes. As for the other classes, they contain large almost-spherical matter clumps. Objects with these features are classified as 'irregular'.

Irrespective of the classification, most of our filaments contain spherical clumps that have low average overdensities (around 20–50) and temperatures (around 0.1 keV). Furthermore, they have radii smaller than 1 Mpc and masses around $10^{12}\,{\rm M}_\odot$ or lower. They can thereby be considered as proper sub-structures of filaments, at least at the resolution we can achieve.

According to the above simple classification, we have estimated that about 30 per cent of the filaments in our simulation box can be classified as 'giant bridges', while approximately 36 per cent are 'branchy'. 'Long-thin' objects are less frequent, but still account for 12 per cent of the filaments. 'Irregular' objects represent 16 per cent of the population. It must be stressed that this classification is performed visually on a limited sample of large objects (about 100 objects longer than 7 Mpc), while smaller objects tend to be more difficult to classify, as resolution effects coarsen their substructures and smooth out their shape.

The remaining objects comprise isolated clumps emerging from the gravitational collapse process and spurious leftovers of the filament reconstruction, in particular at the edges of our boxes (see also Section 4.2). This also affects the low-mass end of the Mass–Temperature (M–T) relation as will be discussed in the following sections.

4.2 Statistical properties of the filaments

Fig. 7 shows the distribution of the gas mass of filaments versus volume. Most objects fall along a narrow scaling relation, fitted by $V \approx 1000\,{\rm Mpc}^3 \times M/(2\times10^{14}\,{\rm M}_\odot)$. For comparison, we also show the best-fitting relations for the case of galaxy clusters, extracted from the 2-1_1024 and 2-c1_1024 runs (for a total of ∼300 objects in the gas-mass range $10^{12} \leq {\rm M/M}_\odot \leq 10^{15}$). Independent of resolution and physics, a self-similar scaling relation for filaments is found, as for galaxy clusters, yet with a higher normalization. However, the normalization of the best fit is smaller for the runs with efficient cooling ('c1' models), implying that cooling produces significantly more compact filaments, and that this removes more volume from the WHIM phase and locks it into overcooling haloes, in turn reducing the volume of the filaments.

Fig. 8 gives the distribution of gas mass versus the length of each filament, which is approximated using the diagonal of the bounding box defined by the reconstruction algorithm (Section 3). The distribution for the full sample of each run is also described by a well-defined power law with a rather narrow dispersion of values around the mean, and with a self-similar scaling with mass, $L \propto M^{1/3}$. The presence of unresolved small-sized haloes embedded within irregular filaments can artificially steepen the relation by increasing the total mass of gas in filaments, while for higher masses their contribution becomes negligible. Therefore, we also show the distribution and best fit (which become just a bit steeper, but still consistent with the $\propto M^{1/3}$ scaling) for the distribution of filaments limited to $\geq 10^{13}\,{\rm M}_\odot$ objects, which are characterized by $L \geq 10$ Mpc. However, notice that our method systematically underestimates lengths, hence this trend represents a lower bound for the mass–length relation. The runs with cooling show a rather steeper scaling, suggesting that filaments of the same length are less

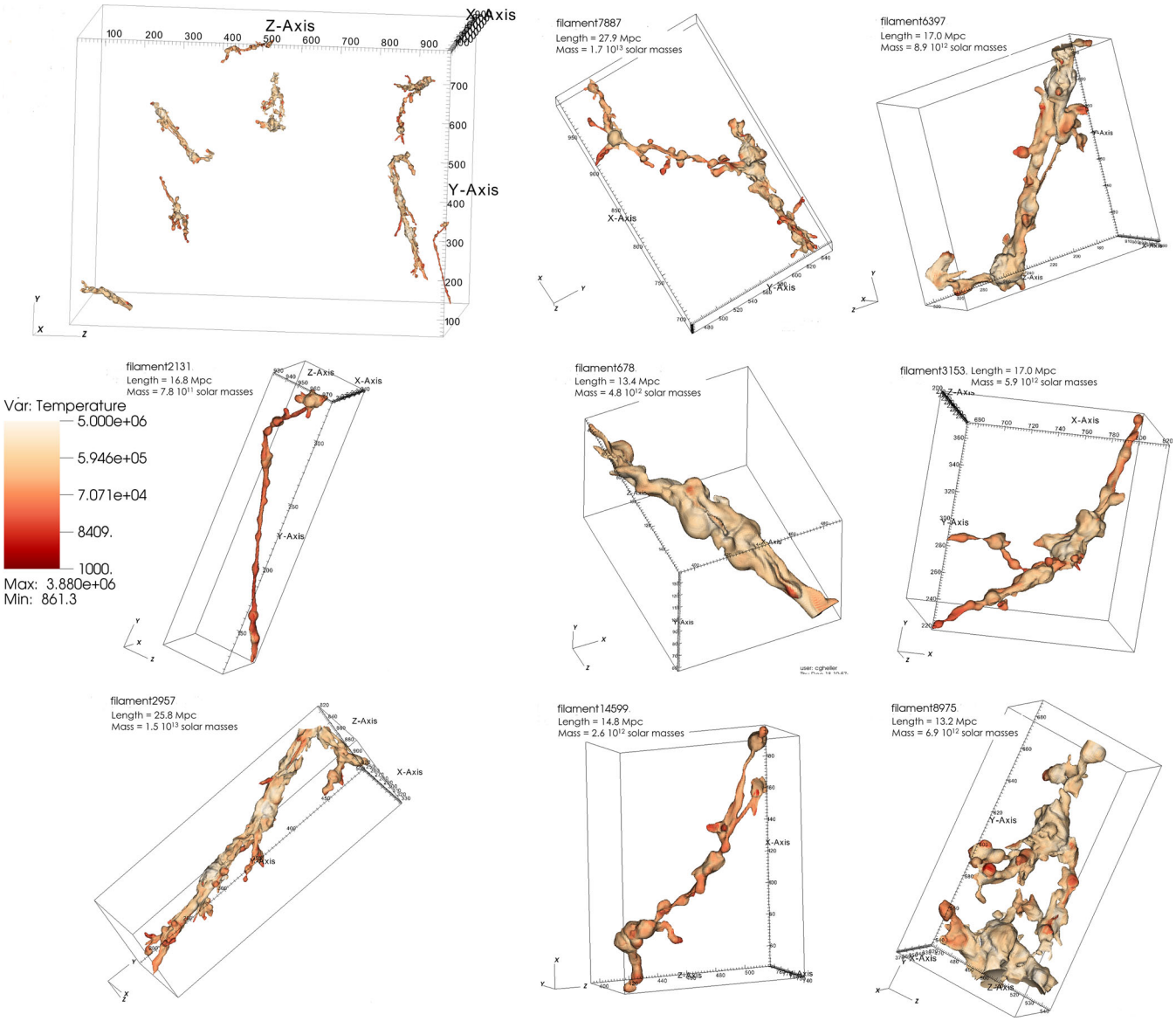

Figure 6. Eight filaments selected from simulation 3-1_1024. Each object is identified by a different ID (an integer number). The top left panel shows the selected filaments altogether in the simulation box, for comparison. The other panels are close-ups on each single filament. Colours represent the gas temperature in the outer surface of each object.

massive than in non-radiative runs. This is easily explained by the mass drop-out of cooling gas on to clumps within filaments, which can significantly remove a fraction of the WHIM from the most diffuse phase, and at the same time promote the full collapse of small-sized haloes and their detection by our algorithm.

The radii of the filaments, presented in Fig. 9, are estimated assuming cylindrical symmetry, such that $R = (V/\pi L)^{1/2}$, where R, V and L are the radius, the volume and the length of the filament, respectively. This is a rough estimate since many objects are far from a simple cylindrical geometry. However, it provides an indication of the characteristic transversal size of a filament and its distribution with mass, with radii between 0.1 and 0.3 Mpc for objects up to 10^{12} $M_\odot$, growing to more than 1 Mpc for the largest filaments, with masses between 10^{14} and 10^{15} $M_\odot$. If resolution is increased, the radii of filaments shrink, as indicated by comparing the 1-0_1024 and 1-1_1024 to the 1-1_2048 interpolation fits. This affects in particular smaller objects, as shown by the right panel of Fig. 9, where we present the radius–mass relation for the sub-set of filaments with masses above 10^{13} $M_\odot$. The transverse size of these large filaments is less affected by resolution. This indicates that the properties of those objects whose radius is comparable to the cell size (low mass filaments) are not fully converged with spatial resolution. Also radiative cooling (run c1) leads to narrower filaments, with the smallest radii associated with 3-c1_1024 and 1-c1_1024. This effect is compensated by the efficient AGN feedback in the c2 models.

For the same objects, we show in Fig. 10 the relation between the enclosed gas mass and the volume-averaged gas temperature. Here a less defined scaling relation is seen. The overall distribution follows a scaling law similar to galaxy clusters in the non-radiative case ($T \sim M^{2/3}$), with an $\sim$1 order of magnitude lower normalization. However, a small fraction of the identified objects has unexpected properties, with low masses (below 10^{12} $M_\odot$) and high temperatures above 10^5 K). These outliers are due to our reconstruction

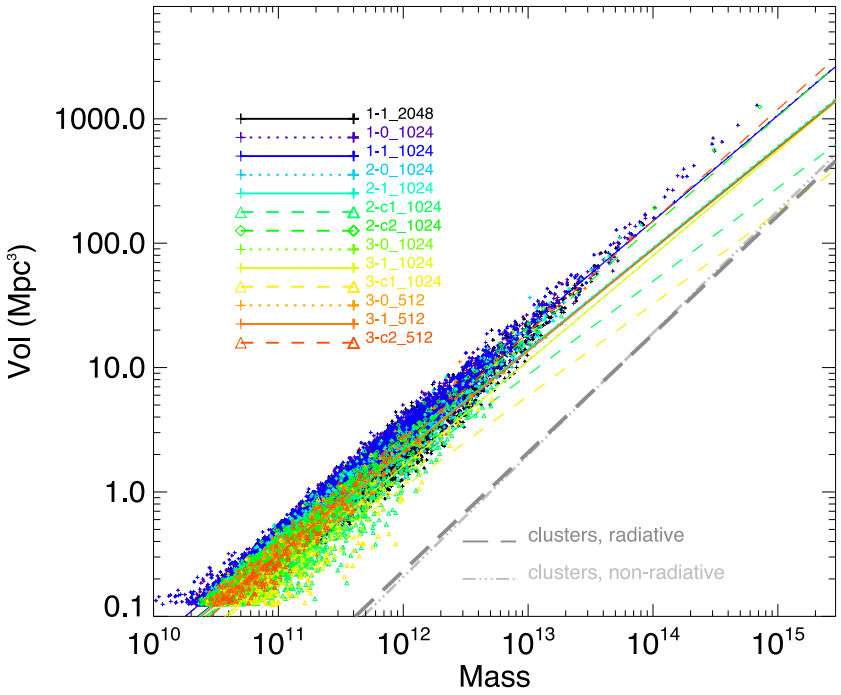

Figure 7. Relation between the enclosed gas mass and volume for the filaments in our sample (only 1/20 of filaments are shown for each model, for a clearer view). The additional lines in colour show the best-fitting relation within each sample, while the two grey lines show the best fit for the population of galaxy clusters extracted from run 2-1_1024 and 2-c1_1024.

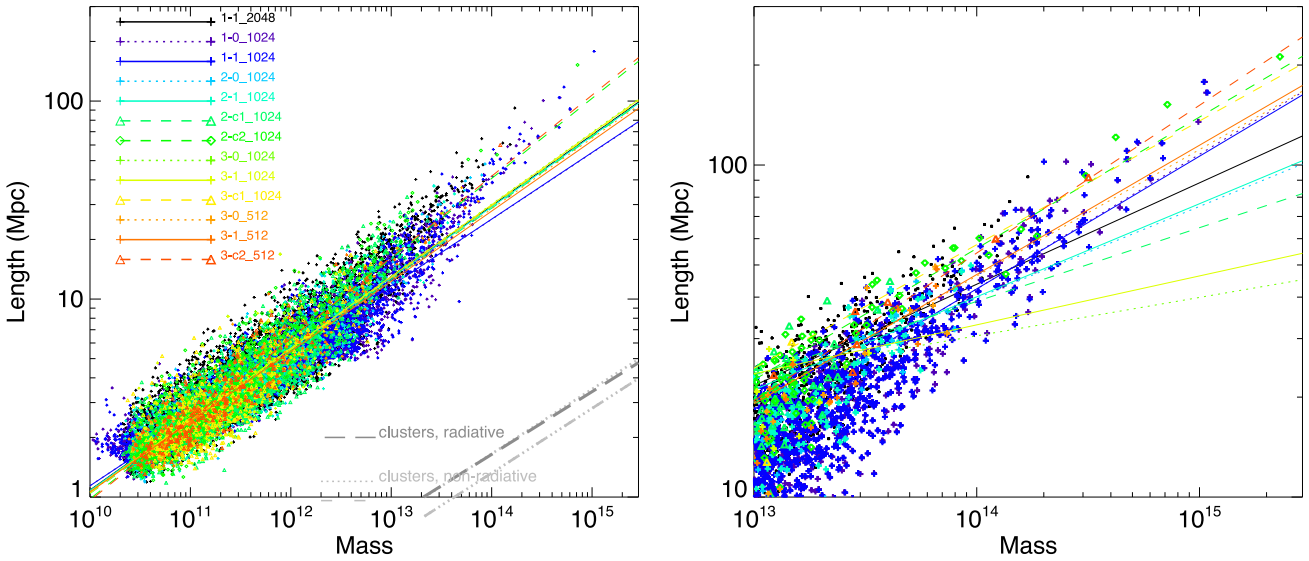

Figure 8. Relation between the enclosed gas mass and the estimated length of filaments in our sample. The left panel shows the full range of values in the data set (only 1/20 of filaments are shown for each model, for a clearer view). The additional lines in colour show the best-fitting relation within each sample. The right panel only focuses on the objects with mass $M \geq 10^{13}$ $M_{\odot}$ (in this case all objects are plotted; same colour coding as in the left panel). The length of each object is an estimate based on the bounding box of each filament, as described in Section 3.

procedure, which does not support periodic boundary conditions. They correspond to small leftovers of larger (and hotter) objects crossing one of the sides of the computational box and there cut in two distinct parts.

Variations of CR physics produce extremely small effects, and the scaling relations are essentially the same for the '1' and '0' models. Instead, the role played by gas cooling and feedback from AGN becomes much more relevant compared to the previous scaling relations since temperature is directly affected. As for galaxy clusters, runs including cooling and AGN feedback produce a steepening of the scaling relation in the low-mass end of the distribution. Due to cooling, the average temperature at all masses is reduced significantly, and also the best-fitting relations for the runs including cooling are steeper than in the non-radiative case. The effect is even bigger than in the case of galaxy clusters, as shown by Fig. 10, comparing the best fit for clusters and filaments in the same volume.

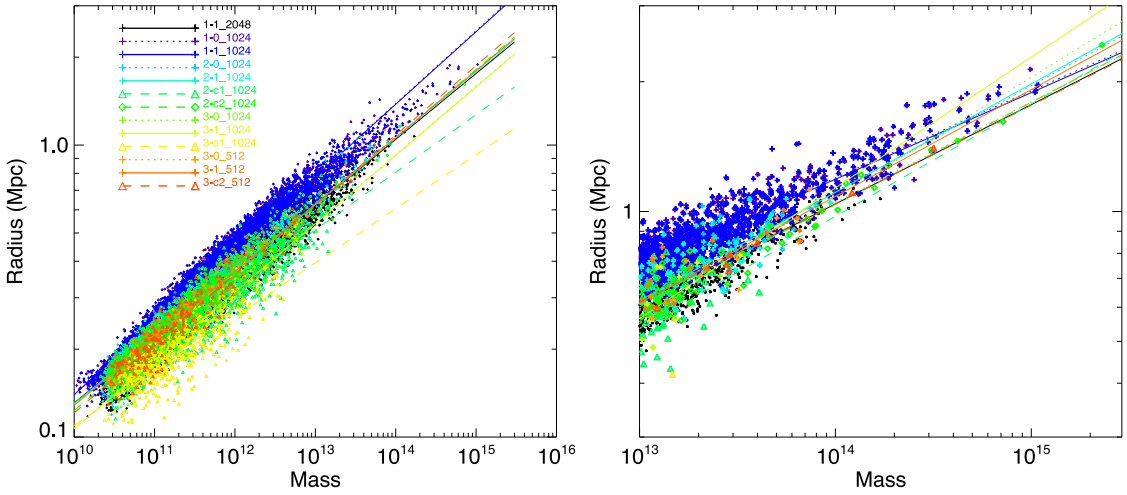

Figure 9. Relation between the enclosed gas mass and the estimated radius of filaments in our sample. The left panel shows the full range of values in the data set (only 1/20 of filaments are shown for each model, for a clearer view). The additional lines in colour show the best-fitting relation within each sample. The right panel only focuses on the objects with mass $M \geq 10^{13}\,\mathrm{M}_{\odot}$ (in this case all objects are plotted, same colour coding as in the left panel). The fit for the 3-c1_1024 model is omitted since statistically not meaningful (too few points available in the selected mass range). The radius of each object is estimated assuming cylindrical symmetry, as $R_{\rm fil} = (V/\pi L)^{1/2}$, where V and L are the volume and the length of the filament, respectively.

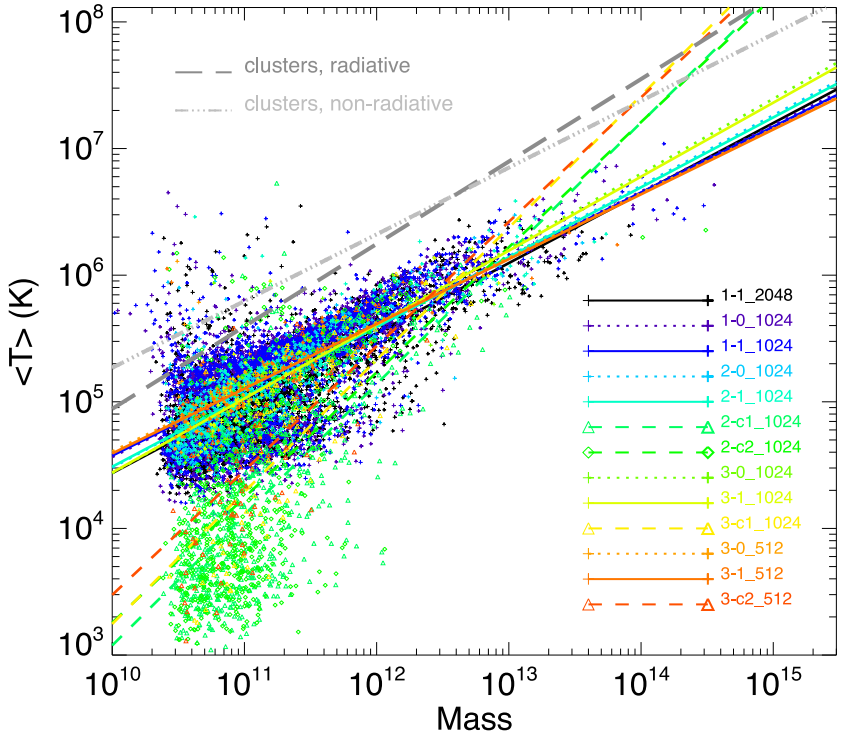

Figure 10. Relation between the enclosed gas mass and the average temperature for the filaments in our sample (only 1/20 of filaments are shown for each model, for a clearer view). The additional lines in colour show the best-fitting relation within each sample, while the two grey lines show the best fit for the population of galaxy clusters extracted from run 2-1_1024 and 2-c1_1024.

This can be explained considering that first, below $T \leq 10^5$ K, the radiative cooling is strongly affected also by line cooling and second that although AGN feedback is effective within clusters and can reach out to the WHIM in filaments, it is obviously less efficient there given the distance (several $\sim$ Mpc) from its release. As also pointed out in the next section, the cooling efficiency in this regime is probably overestimated in our case, since we assumed a (constant) metallicity of $0.3\,\mathrm{Z}_{\odot}$ everywhere in the simulated volume. Furthermore, the mass dropout into forming stars is not included.

The volume/mass/temperature number distributions for all objects are given in Figs 11–13. Apart from a deficit of objects with $V \leq 1$ Mpc^3 in the 1-0_1024 and 1-1_1024 runs (due to coarse resolution effects; Section 3.3), the volume distribution of objects is very similar in all runs and is described by a simple $\log_{10}(\mathrm{N_{fil}}) \propto \mathrm{V}^{-1}$ relation across $\sim$3 decades in volume (Fig. 11). The various curves show a good numerical convergency down to gas masses of $\sim 10^{11}\,\mathrm{M}_{\odot}$, indicating that our reconstructed distribution of objects is complete down to this mass. The total volume occupied

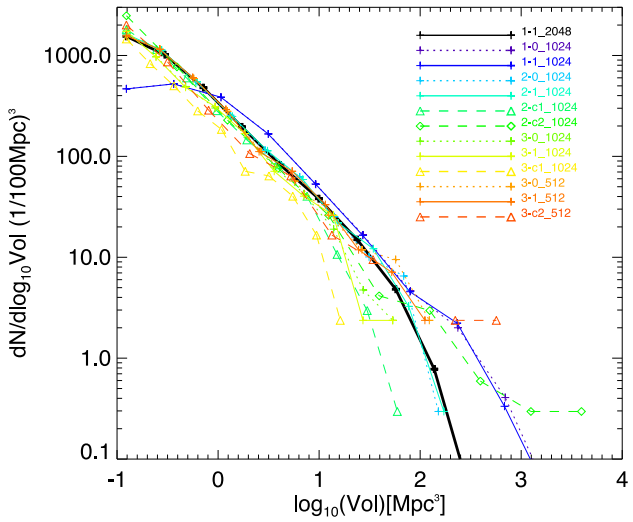

Figure 11. Number of filaments normalized to 100 cubic Mpc as a function of their volume.

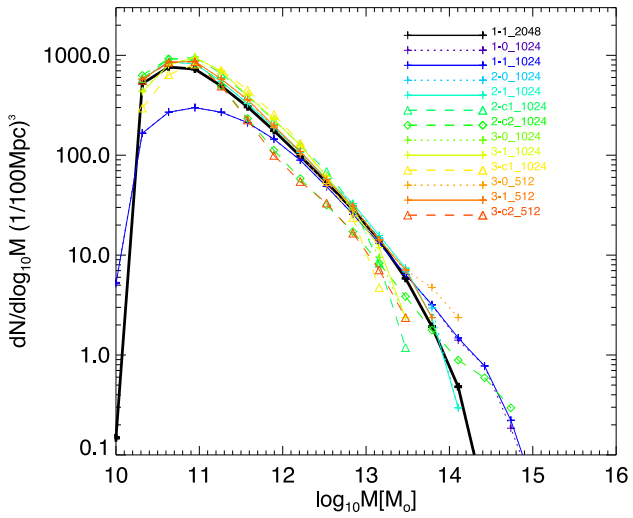

Figure 12. Number of filaments normalized to 100 cubic Mpc as a function of their gas mass.

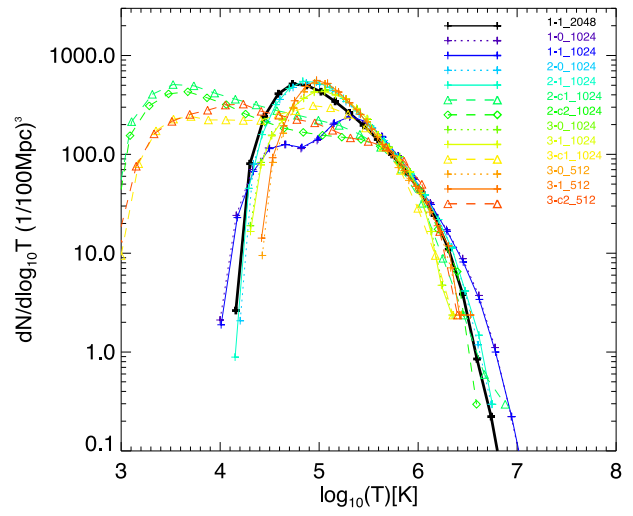

Figure 13. Number of filaments normalized to 100 cubic Mpc as a function of average temperature.

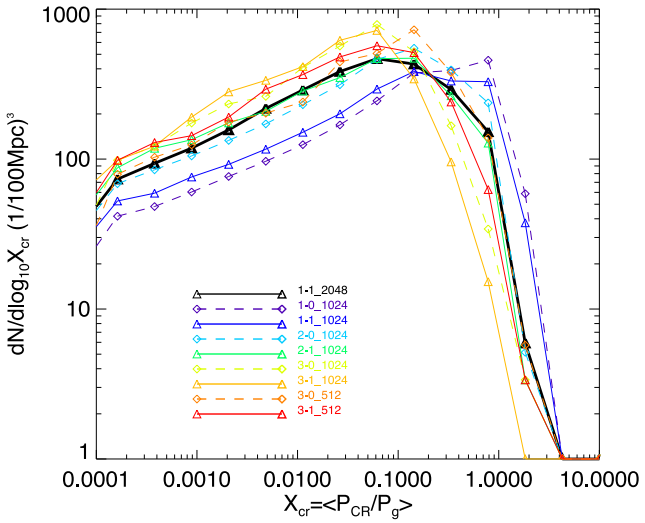

Figure 14. Number of filaments normalized to 100 cubic Mpc as a function of the pressure ratio between CR energy and gas energy.

by filaments ranges from 3.8 to 4.5 per cent of the computational volume in all our runs.

When physical resimulations of the same volume are compared, we find a significant excess of large-volume filaments when the more efficient 'c2' feedback model is used, for $\geq$100 Mpc^3 as well as a significant deficit of haloes in the range 10 Mpc^3 $\leq V \leq$ 100 Mpc^3. This is due to the powerful AGN feedback at high redshifts, which leads to the expulsion of gas from the centre of dense proto-clusters and affects the properties of a few tens of massive filaments around the most massive haloes in the box. The efficient feedback releases hot gas beyond the radius achieved by non-radiative runs, with a strong impact on the densest regions, where the AGN feedback mostly takes place. This enriches even rarefied environments with additional gas, and leads to the junction of otherwise disconnected structures through the extra gas. A more detailed analysis will be given in the next section (e.g. Fig. 16).

On the other hand, the effect of radiative cooling is enough to produce more compact objects within filaments than in the non-radiative case, thereby causing an increase of the low-volume objects in the sample. Both effects are relevant for any filament detection scheme based on gas. Very similar trends are found for the distribution of filament mass (Fig. 12). We conclude that on average only one filament with $M \geq 10^{14}$ M$_\odot$ and $V \geq 1000$ Mpc^3 is found within a volume of (100 Mpc)^3, while within the same volume we can find $\sim$10 objects with $M \geq 10^{13}$ M$_\odot$ and $\sim 10^2$ objects with $M \geq 10^{12}$ M$_\odot$.

The distribution of temperatures (Fig. 13) clearly shows the imprint of radiative cooling on the WHIM. Cooling removes a significant part of the cosmic population of filaments from the soft X-ray bands and pushes it much below 10^5–10^6 K (still above the minimum level set by our assumed UV heating background, which had dropped off at a level of a few $\sim 10^2$ K at $z = 0$), as already seen in the average temperatures in Fig. 5. The coarse resolution in the 1-0_1024 and 1-1_1024 runs is responsible for an excess of large temperatures compared to the other runs with a higher resolution.

Finally, we calculate the ratio between the thermal gas pressure and the pressure of CR-protons accelerated by shock waves, as in Vazza et al. (2014a). Fig. 14 gives the number distribution of filaments and compares all our '1' and '0' models for the non-radiative case. For the bulk of the population the pressure ratio

within the volume of filament is $P_{\rm CR}/P_{\rm g} \sim 0.1$–$0.2$, with a tendency of larger filaments to have lower ratios. As expected, the lower efficiency '1' model (Kang & Ryu 2013) produces a smaller CR pressure compared to the higher efficiency '0' model (Kang & Jones 2007), However, the differences are small. At the same resolution, the two distributions differ by ∼20–30 per cent. This is expected because in the different simulations the enrichment of CRs into filaments is equally strong, owing to the fact that the saturated efficiency of the two acceleration models is only different by a factor of ∼30 per cent in our treatment (Vazza et al. 2014a). The effect of increasing resolution is to lower the average pressure ratio due to the overall weakening of shocks, which is made manifest by the shift of the peak of this relation to lower values, going from the coarse 1-0_1024 and 1-1_1024 runs (where the number of objects is also found to be smaller than in the other runs) to the 3-0_1024, 3-1_1024 and 3-c1_1024 runs. This suggests that very large values of the pressure ratio are mostly driven by resolution effects on the shock population (Ryu et al. 2003; Vazza et al. 2011). However, thorough investigations on resolution effects in the distribution of CRs in these runs have been already presented Vazza et al. (2014a, fig. 11) and showed that $P_{\rm CR}/P_{\rm g}$ is a rather well-converged quantity (within a factor of ∼2–3) for all across the full range of cosmic environment, for spatial resolution equal or better than ∼200-300 kpc, i.e. well in the range of that explored by the runs we use in this work. Overall, these findings are in agreement with Vazza et al. (2014a), and indicate that, provided diffusive shock acceleration (DSA) can take place at low overdensities, cosmic filaments can store a large amount of CRs.

4.3 Properties of individual filaments

In order to monitor the impact of non-gravitational physics (cooling and feedback from AGN) on to filaments, we analysed the properties of individual objects. For this purpose, we extracted from the 3-1_1024 and 3-c1_1024 runs all cells belonging to two objects: filament 'F1' with a length of ∼15.5 Mpc and filament 'F2' ∼10.2 Mpc long. The maps of projected gas temperatures for these objects are shown in Fig. 16. For the two different physical models, the filaments' morphologies are quite similar. However, the combined effect of radiative cooling and feedback produces more substructures within each filament which are narrower compared to the non-radiative runs. Also, the presence of more compact sub-haloes causes a higher fragmentation in several portions of the filaments in the radiative runs.

Other thermodynamical differences are more conspicuous in phase diagrams, as in the (T,ρ) phase diagrams of Fig. 15. The properties of the cells in filaments can be compared to the global phase diagram of the larger $\approx(35\ \ {\rm Mpc})^3$ boxes containing the two filaments, in order to compare with the phase diagram of cosmic baryons in the volume. The two objects show a very similar thermodynamic pattern and contain most of the dense and WHIM ($T \leq 10^7$ K) outside galaxy clusters. Most of the volume in these two objects is taken up by gas with densities $\rho \sim 10\langle\rho\rangle$ and temperature $T \sim 10^6$ K. The combined action of cooling and feedback is relevant in both cases. Cooling promotes the formation of denser clumps in both filaments (visible as horizontal stripes on the phase diagrams), and it is found to affect the filaments even at $T \leq 10^7$ K, i.e. in a regime where metal cooling can be dominant and that future X-ray telescopes (e.g. ATHENA, Nandra et al. 2013) will probe. Although recent observations of metallicity at the edge of the Perseus cluster found a mean metallicity of the order of ∼0.2–0.3 $Z_\odot$ (Urban et al. 2014), our assumption is likely to overestimate the presence of metals at early times, and translates into an upper limit on the amount of radiative cooling of the WHIM (e.g. Cen & Ostriker 2006; Maio et al. 2011; Smith et al. 2011).

At the same time, the effect of feedback from the nearby clusters is enough to increase the temperature by a factor of 2–3 in most of the volume compared to the non-radiative run. The most peripheral parts of some clusters expand due to the AGN outbursts and, by getting more rarefied, are identified as part of filaments by our algorithm (this is particularly evident in the upper part of filament F2.). This leads to a slight increase in the size of the structure due to percolation of expanding shells of matter, which in turn enhances the maximum length of several filaments in our radiative runs (as also pointed out in Section 4.2).

The effect of our prescription for the thermal feedback and the fact it reaches out to the outer part of filaments is similar to what is reported by other authors, who investigated similar feedback schemes (Kang et al. 2007; McCarthy et al. 2010).

In each of the two objects, we computed the location of the spine along the major axis of the filament and computed the profiles transverse to it. The spine is computed by first identifying the major axis of each structure (based on the bounding box of each object, as in Section 3.1) and then computing the centre of gas mass in consecutive slices (each one cell thick) perpendicular to the main axis, as shown in Fig. 16. Figs 17 and 18 show the profiles of gas density, temperature and enclosed gas mass transverse to the main axis of the filaments, out to $r_{\rm fil} \sim 3.3$ Mpc (F1) and 2 Mpc (F2). Since the transverse size of each object might vary along the spine (Fig. 16) our radial bins are normalized to the transverse size of the filament along the spine, i.e. we bin our profiles according to $r/r_{\rm fil}$, where $r_{\rm fil}$ is defined as the minimum distance of the filament edge from the spine in the corresponding transversal plane. The density profiles for the same physical model are rather similar. In the non-radiative case, the central mass density is several $\sim 10^{-28}$ g cm^{-3}, becoming approximately two to three times larger in the radiative case, due to the higher compression. The mass density smoothly drops by a factor of ∼5–10 at $0.5r_{\rm fil}$ from the spine of each filament, then slowly declining outwards. Notice that the density at the last radial bin is larger than our fiducial threshold density ($a_{\rm fil}$) due to the averaging at $r = r_{\rm fil}$ which can include cells with mass density above the threshold resulting from the compression produced by strong external shocks. In all cases the central temperature is around $\sim 10^6$K. However, the corresponding radial profiles are remarkably different. The F1 non-radiative filament shows a gently increasing temperature up to its external boundaries where most of shock heating takes place. The same F1 object is highly affected by AGN feedback and cooling, which leads to a higher central over-density and to a higher temperature peak $\sim 0.5r_{\rm fil}$ from the spine of the filament. The effect is less evident in filament F2. The horizontal lines show the mass cut-off induced by different settings of the $a_{\rm fil}$ parameter. It is clear how setting $a_{\rm fil} > 2$ significantly limits the fraction of gas mass assigned to filaments. This is confirmed by Fig. 18 that shows the cumulative gas mass for the various filaments and models, showing that most of the mass is contained at large distances from the spine, $\geq$0.3–$0.5r_{\rm fil}$ (i.e. ≥700–1500 kpc) and how only using $a_{\rm fil} \leq 2$ this mass can be fully captured by our algorithm. Furthermore, as evident in the temperature profiles, we thus trace the filament out to the position of the main shock fronts including most of the cell that have undergone compression and heating.

In the panels of Fig. 19 we present the profiles of the gas pressure, the CR pressure, the pressure ratio and the shock Mach number for the same objects and runs. In both objects, the thermal gas pressure is

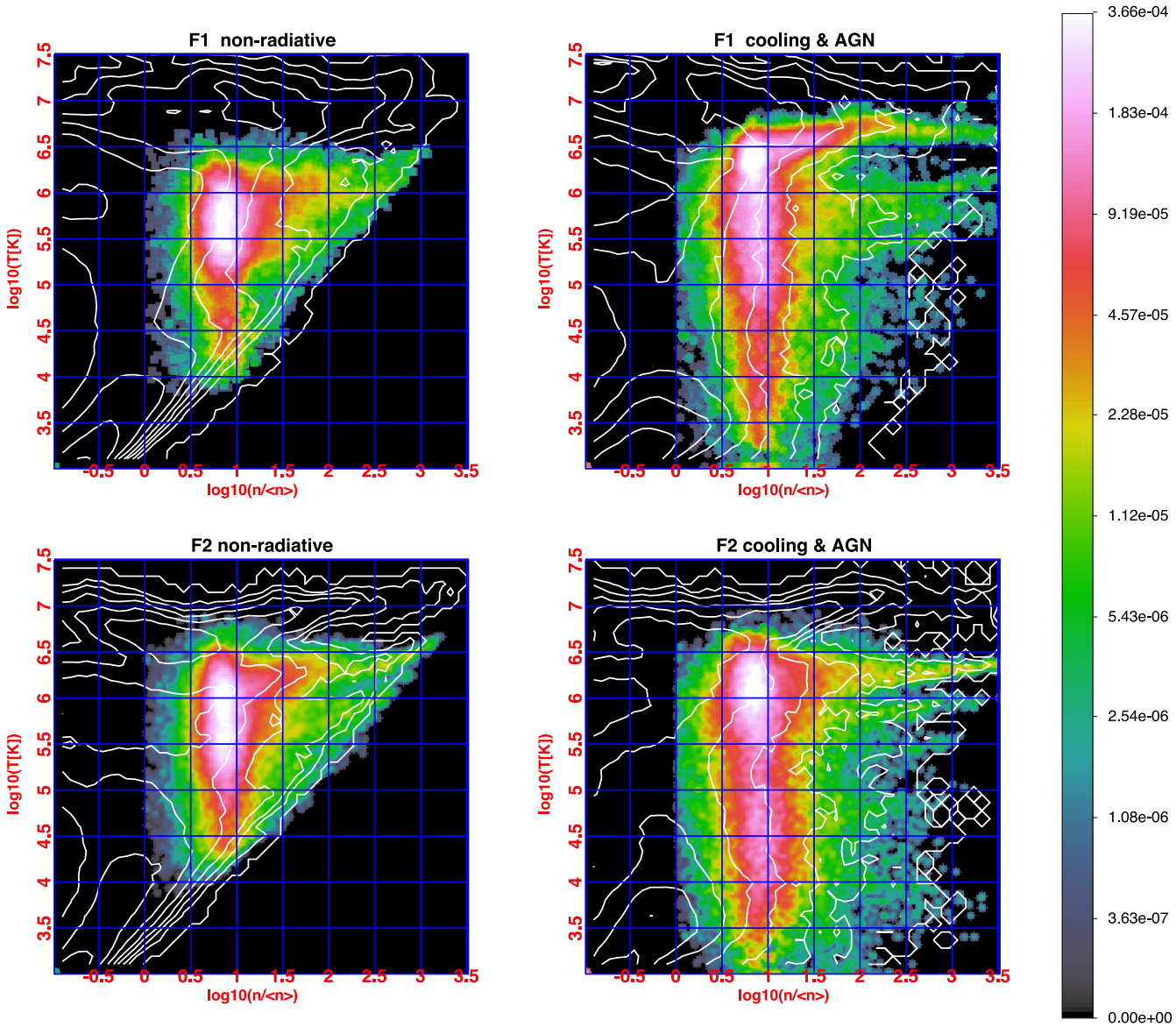

Figure 15. Phase diagram (ρ,T) for the filaments F1 (top panels) and F2 (bottom panels), comparing the non-radiative run and in the cooling and feedback run (c2). The colour coding gives the fraction of volume characterized by a given phase. For each object we also show the contours of the phase diagram for a larger $\approx$(35 Mpc)^3 box in order to compare with the entire distribution of cosmic baryons.

dominant at all radii compared to the CR pressure. However, the CR pressure becomes ∼10–20 per cent of the thermal pressure at large radii in the non-radiative runs, and ∼40–80 per cent of the thermal pressure in the cooling and feedback runs. The latter is a combined effect of the decreased gas temperature and of the stronger shocks (as an effect of additional feedback bursts) in most of the filament volume, which yield a more efficient injection of CRs from DSA. However, inside most of the filament the gas motions are supersonic (Ryu et al. 2008b; Vazza et al. 2014b) and that, therefore, both gas and CR pressure are subdominant compared to the ram pressure of the gas.

Future radio telescopes (such as SKA or, in the nearest future, LOFAR) will be able to investigate this regime and might provide new clues about the degree of plasma collisionality and CRs in this environment, by directly imaging the morphology of strong accretion shocks in radio. One significant emission channel for CRs is represented by direct synchrotron radiation by accelerated CR electrons at strong shocks (Brown 2011; Araya-Melo et al. 2012). In this case, also the level of large-scale magnetization will affect the chance of detection, and present uncertainties about the WHIM leave room for several scenarios (Ryu et al. 2008a; Donnert et al. 2009; Vazza et al. 2014b).

5 DISCUSSION

Compared to previous work (see Section 1) that studied the distribution of DM in the cosmic web (mostly using DM-only simulations), our work focused on the thermodynamic characterization of the baryon component of the cosmic web.

The methods that we have used are particularly sensitive to gas densities close to the average cosmic value and have no artefacts caused by a particle-based DM distribution that especially affect poorly sampled low-density regions. As a consequence, the average overdensity of our population of filaments is smaller than what has

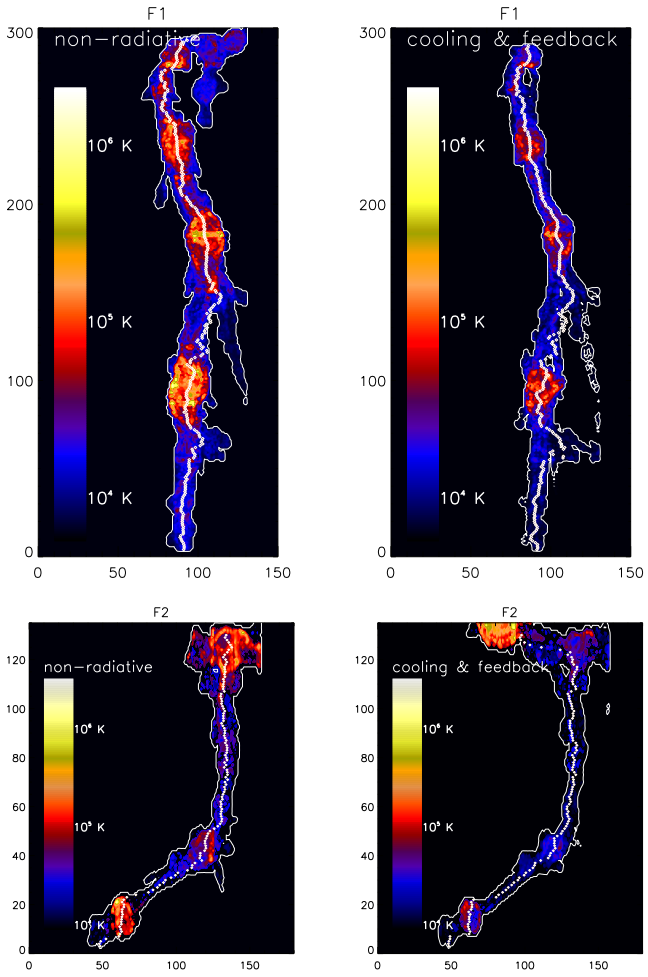

Figure 16. Maps of projected temperature for filaments F1 and F2, for both non-radiative (left) and cooling and feedback (right) runs. The white contours give the boundaries of the filaments as reconstructed by our algorithm, while the white points show the spine of each filament, that we used to compute the profiles in Figs 17–19. Each panel has axes in cell units (here $\Delta x = 74$ kpc).

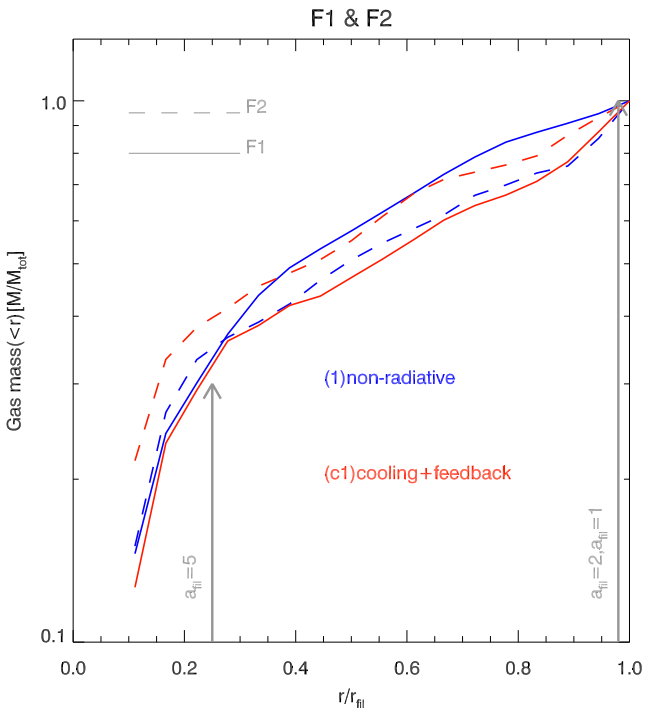

Figure 18. Transverse profile of the enclosed gas mass for the filaments F1 (solid) and F2 (dashed), in the non-radiative run and in the cooling and feedback run (c2). The grey arrows show the approximate location where the mean density profile of filaments is equal to the different values of the density thresholds $a_{\rm fil}$. The profile of each filament has been normalized for the total enclosed mass to the last radial bin.

been quoted in the literature (e.g. Colberg, Krughoff & Connolly 2005).

This procedure enables us to extract the cosmic web down to an overdensity very close to the critical density and to segment it into its filamentary components. Thus, we can analyse a large dynamic range in the mass/volume distribution of filaments, using the recent 2048^3 and 1024^3 grids produced by our group (Vazza et al. 2014a). This led to the extraction of a very large number of

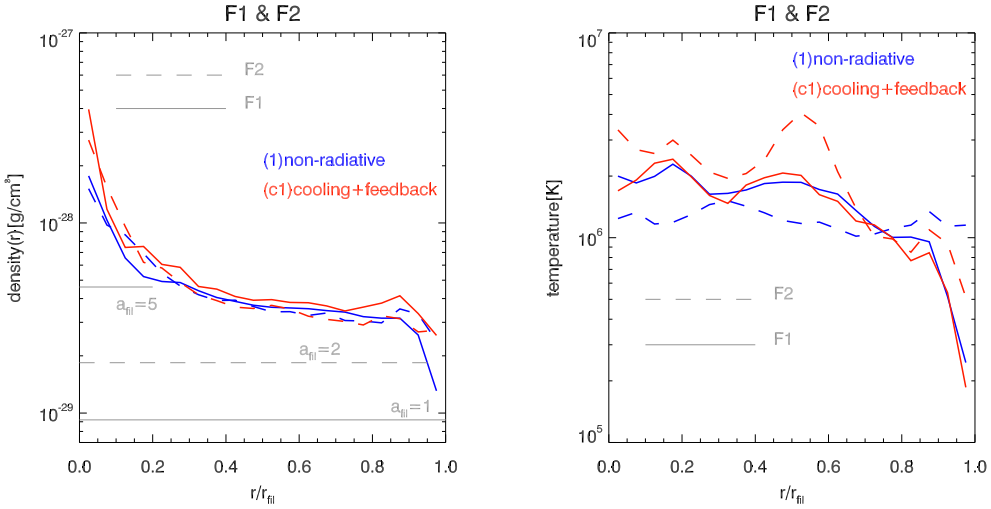

Figure 17. Transverse profile of gas density (left) and gas temperature (right) for the filaments F1 (solid) and F2 (dashed), in the non-radiative run and in the cooling and feedback run (c2). The horizontal lines in the first panel show the density threshold corresponding to different values of $a_{\rm fil}$ (Section 3.3). The radial coordinate is normalized to the transversal size of each filament along the spine (see Section 4.3).

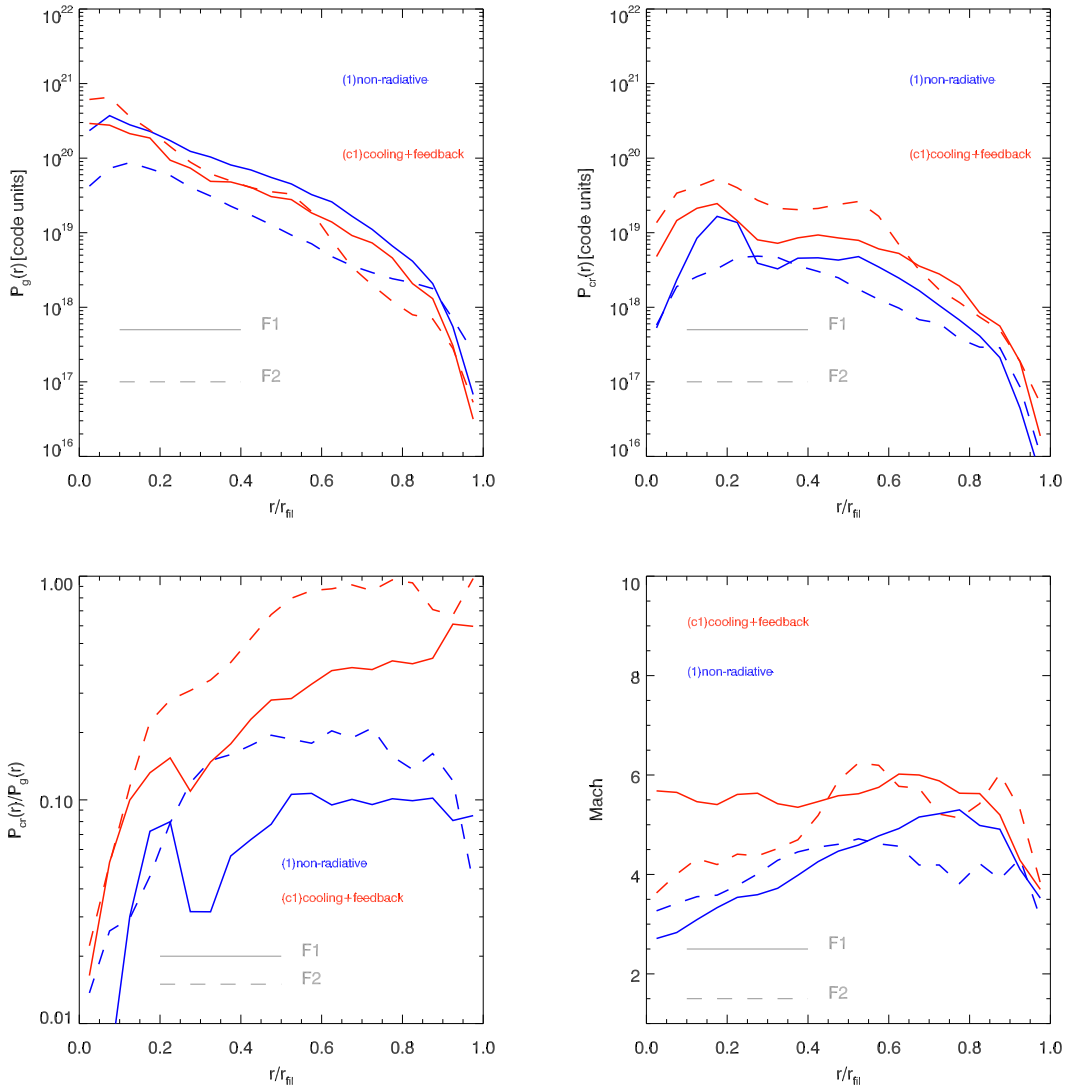

Figure 19. Transverse profiles of gas pressure (top left), CR pressure (top right), pressure ratio (bottom left) and shock Mach number (bottom right) for filaments F1 and F2, for the non-radiative run and in the cooling and feedback runs.

filaments at high resolution, e.g. ∼30 000 objects in our 300^3 Mpc^3 volume, significantly higher than what is typically found in DM-only simulations.

Our method is simpler than other algorithms discussed in the literature (e.g. Stoica et al. 2005; Aragón-Calvo et al. 2007; Hahn et al. 2007; Sousbie et al. 2008; Cautun et al. 2014; Aragón-Calvo et al. 2010; González & Padilla 2010) and is likely prone to possible misidentification in several pathological cases as, for instance, for irregular filaments (see Section 4.1) that in some cases may actually be parts of sheets with density comparable to that of filaments. It can also be affected by resolution effects, e.g. in small clumps whose typical size is close to the resolution limit. However, a recent comparison has shown that the volume occupied by filaments (and, to a lesser extent, the mass locked into filaments) can in principle be measured equally well by both density-based and more sophisticated methods (Cautun et al. 2014). We conclude that, while additional checks might be necessary to assess the nature of specific low-mass/size objects (e.g. also accessing the DM properties of small objects), in general our method gives robust results.

We find that the total volume occupied by filaments ranges from 3.8 to 4.5 per cent of the computational volume, which is consistent with the range provided by Cautun et al. (2014), and significantly smaller than what is found by previous *N*-body simulations (e.g. Hahn et al. 2007; Aragón-Calvo et al. 2010). The largest objects identified in our data set have a mass and estimated length of the order of what is found by large *N*-body simulations (e.g. Colberg et al. 2005; Cautun et al. 2014), provided that we rescale our gas masses by the cosmic baryon fraction in order to get the total mass (which is legitimate here since at the typical filaments' over-density the baryon fraction is close to the cosmic baryon fraction). However, the mass distribution of filaments in the cosmic volume (Fig. 12) shows a more extended power-law behaviour down to the smallest masses compared to the literature (e.g. Cautun et al. 2014, fig. 53). Here we can measure an unbroken power-law distribution in the range 10^{11}–10^{14} M$_\odot$, suggesting that our sample of filaments is complete down to total masses of 6×10^{11} M$_\odot$, i.e. 1–2 orders of magnitude deeper than what is typically achieved with *N*-body simulations.

We also performed an analysis of the properties of individual filaments, focusing on two massive objects as representative cases. The profiles of gas density across the filaments is similar to what is reported elsewhere (Colberg et al. 2005; Dolag et al. 2006;

Aragón-Calvo et al. 2010). The description of sharp discontinuities of the temperature at the outer accretion shocks is a feature in which our simulations are particularly effective. Qualitatively similar results for the density and temperature profiles were reported by Klar & Mücket (2012), but these were based on idealized simulations of a forming filament that were not set in a cosmological framework. The pattern of strong accretion shocks surrounding filaments are consistent with previous works in the literature (Ryu et al. 2003; Skillman et al. 2008; Vazza, Brunetti & Gheller 2009; Vazza et al. 2011; Araya-Melo et al. 2012), which also predict high CR-acceleration efficiency at the scale of filaments (Pfrommer et al. 2006). Based on our run-time modelling of CR physics (Vazza et al. 2014a), the pressure ratios within filaments show that CRs can contribute up to ∼10–20 per cent of the total pressure. However, the present uncertainties CR-acceleration efficiencies, especially in (low-density) environments (e.g. Kang & Ryu 2013), force us to treat this number with caution. The impact of radiative cooling and feedback from AGN on the WHIM has been explored by several authors (e.g. Cen & Ostriker 2006; Roncarelli et al. 2006; Hallman et al. 2007). Still, as far as we know, our work represents the first study of how cosmic filaments change with feedback. However, our modelling of radiative cooling overestimates the gas metallicity at high redshift, and possibly also in the outer parts of filaments at low redshifts, even if the observational constraints are still weak (e.g. Urban et al. 2014).

6 CONCLUSIONS

In this work we investigated the main properties of the baryonic matter in cosmic filaments by using a large set of cosmological grid simulations recently obtained with the ENZO code (Vazza et al. 2014a). We built a filament identification procedure upon the VisIt data analysis and visualization software, exploiting a combination of its *Isovolume* and *Connected Components* algorithms. The method separates over-dense from under-dense regions, identifying a filament as a connected set of cells with mass density above a given threshold, $a_{\rm fil}$. The filament identification is further refined by eliminating clusters and small clumps and accepting only elongated objects. The resulting methodology depends on six parameters, the most important being the mass density threshold $a_{\rm fil}$, whose value lies in the range 0.5–2.0. The exact value can influence some statistical properties of the identified objects (e.g. the maximum size of filaments extracted from a simulation). Other properties (e.g. the average density within filaments) are unaffected. The remaining parameters are either more tightly constrained or have only a minor impact on the results (see Appendix A for further discussion).

Our most significant findings can be summarized as follows.

(i) Morphology and thermodynamic properties: filaments, especially long objects (longer than ∼7 Mpc) show a broad variety of shapes and thermodynamic properties that depend on the environment in which they lie and on the evolutionary stage. A first rough visual classification has been attempted, but further investigation is needed to reach comprehensive and robust conclusions.

(ii) Average properties of the WHIM: the population of filament extracted setting $\varrho \geq \varrho_0$ and removing collapsed haloes is of the order of ∼3500 objects within $(100\ {\rm Mpc})^3$. The enclosed gas density averaged over the whole population is ~ 3–$5\ \rho_0$, the average temperature is a few $\sim 10^5$K.

(iii) Scaling relations: filaments follow well-defined scaling relations in the (T, M) and (V, M) plane, with slopes similar to those of galaxy clusters but different normalization (i.e. lower temperature and larger masses). The observed scaling shows that also in filaments gravity sets a clear dependence between the enclosed mass and the gas temperature, $(T \propto M^{2/3})$ even if at low masses the effect of radiative cooling can steepen the relation significantly, similar to the case of radiative galaxy clusters.

(iv) Massive filaments: the most massive objects found in our suite of simulations have gas masses in excess of $\sim 10^{15}\ {\rm M}_\odot$, an average (volume-weighted) temperatures of $\sim 10^7$ K and a total volume of a few $\sim 10^3 {\rm Mpc}^3$, reaching a total length of the order of 100 Mpc. Only about one object of such size can be found on average within $100^3 {\rm Mpc}^3$.

(v) Smallest filaments: the smallest filaments that our algorithm can reliably extract have a length of about 1–2 Mpc, gas mass of a few $\sim 10^{10}\ {\rm M}_\odot$ and temperature of $\sim 10^4$-10^5 K (or down to $\sim 10^3$ K in the radiative case).

(vi) Resolution effects: spatial resolution can affect the population of filaments at all scales. The most evident effect is the high diffusion in low-resolution simulations, which leads to the percolation of otherwise disconnected structures. This leads to a drop of the number of small objects per unit of volume and to an increase in the number of large objects. As a consequence, the same trend can be found in the mass distributions. Temperature distributions show a similar behaviour due also to the largest distance travelled by shock waves in low-resolution simulations, heating up larger volumes. In summary, our analysis on the thermodynamical and statistical properties of the WHIM suggests that a spatial resolution equal or better than $\sim 100\ {\rm kpc}\ h^{-1}$ is necessary to have converging results on the simulated filaments properties, considering objects of masses larger than $10^{10} {\rm M}_\odot$.

(vii) Effects of radiative cooling: cooling (mostly dominated by line cooling here, given the assumed fixed large metallicity) decreases the average temperature of the WHIM by a factor of ∼ 3–5 compared to the non-radiative case. In the presence of small-scale clumps contained in filaments, the minimum temperature inside filaments is reduced by more than an order of magnitude. The gas density profile is also increased by a factor of ∼3 close the axis of filaments in the presence of cooling.

(viii) Effects of AGN feedback: efficient feedback from AGN can affect most of the volume of filaments, even out to large distances from the nearby haloes. The thermal feedback implemented in our model causes the expulsion of gas from haloes and the expansion of filaments, which can percolate and produce significantly larger objects compared to the non-radiative case.

(ix) Effects of CRs: the dynamical impact of CRs is small since where the gas density is higher, close to the axis of filaments, the ratio between CRs and the thermal gas is small (∼10–20 per cent in the non-radiative case). However, the combination of cooling and AGN feedback is found to increase the budget of CRs significantly outwards, where strong accretion shocks dominate.

As a final remark, we stress that a comprehensive description of the observable properties of the cosmic web requires further important physical mechanisms to be taken into account, such as star formation and chemical enrichment of the diffuse medium by galactic activity (which affects the distribution of elements in the WHIM, and determines the emission/absorption properties of the gas through lines; e.g. Cen & Chisari 2011; Nicastro et al. 2013), partial thermal equilibration of the WHIM due to proton–electron equilibration (e.g. Rudd & Nagai 2009), thermal conduction (Klar & Mücket 2012) and large-scale magnetic fields (e.g. Brüggen et al. 2005; Dolag et al. 2008; Ryu et al. 2008a; Vazza et al. 2014b). Such extensive studies will be the subject of forthcoming work.

However, the methodology presented in this paper does not depend on the physics of the problem and can be applied to many kinds of cosmological simulations as is based on simple assumptions. It adapts very well to even larger data sets, and its parallel strategy will allow us to exploit it effectively for the identification and characterization of filamentary structures in any future simulations programme.

ACKNOWLEDGEMENTS

Computations described in this work were performed using the ENZO code (http://enzo-project.org), which is the product of a collaborative effort of scientists at many universities and national laboratories. We gratefully acknowledge the ENZO development group for providing helpful and well-maintained online documentation and tutorials.

We acknowledge PRACE for awarding us access to CURIE-Genci based in France at Bruyeres-le-Chatel. The support of the TGC Hotline from the Centre CEA-DAM Ile de France to the technical work is gratefully acknowledged. We also acknowledge CSCS-ETHZ[4] for the use of the Cray XC30 Piz Daint in order to complete the 2048^3 run and of the Pilatus system for data processing and visualization. FV and MB acknowledge support from Forschergruppe FOR1254 from the Deutsche Forschungsgemeinschaft. FV and MB acknowledge the usage of computational resources on the JUROPA cluster at the at the Jülich Supercomputing Centre (JSC), under project no. 5018, 5056, 6981 and 7006. We would like to thank M.G. Giuffreda for her valuable technical assistance at CSCS.

REFERENCES

Anderson J. C., Garth C., Duchaineau M. A., Joy K. I., 2010, IEEE Trans. Vis. Comput. Graph., 16, 802
Aragón-Calvo M. A., Jones B. J. T., van de Weygaert R., van der Hulst J. M., 2007, A&A, 474, 315
Aragón-Calvo M. A., van de Weygaert R., Jones B. J. T., 2010, MNRAS, 408, 2163
Araya-Melo P. A., Aragón-Calvo M. A., Brüggen M., Hoeft M., 2012, MNRAS, 423, 2325
Bagchi J., Enßlin T. A., Miniati F., Stalin C. S., Singh M., Raychaudhury S., Humeshkar N. B., 2002, New Astron., 7, 249
Bleuler A., Teyssier R., Carassou S., Martizzi D., 2015, Comput. Astrophys. Cosmol., 2:5
Bolton J. S., Becker G. D., Haehnelt M. G., Viel M., 2014, MNRAS, 438, 2499
Bond J. R., Kofman L., Pogosyan D., 1996, Nature, 380, 603
Brown S. D., 2011, JA&A, 32, 577
Brüggen M., Ruszkowski M., Simionescu A., Hoeft M., Dalla Vecchia C., 2005, ApJ, 631, L21
Bryan G. L. et al., 2014, ApJS, 211, 19
Cautun M., van de Weygaert R., Jones B. J. T., Frenk C. S., 2014, MNRAS, 441, 2923
Cen R., Chisari N. E., 2011, ApJ, 731, 11
Cen R., Ostriker J. P., 1999, ApJ, 514, 1
Cen R., Ostriker J. P., 2006, ApJ, 650, 560
Chen Y.-C., Ho S., Freeman P. E., Genovese C. R., Wasserman L., 2015, preprint (arXiv e-prints)
Childs H. et al., 2012, High Performance Visualization–Enabling Extreme-Scale Scientific Insight
Colberg J. M., Krughoff K. S., Connolly A. J., 2005, MNRAS, 359, 272
Colella P., Woodward P. R., 1984, J. Comput. Phys., 54, 174
Courtois H. M., Pomarède D., Tully R. B., Hoffman Y., Courtois D., 2013, AJ, 146, 69
Davé R. et al., 2001, ApJ, 552, 473
de Lapparent V., Geller M. J., Huchra J. P., 1986, ApJ, 302, L1
Dolag K., Meneghetti M., Moscardini L., Rasia E., Bonaldi A., 2006, MNRAS, 370, 656
Dolag K., Bykov A. M., Diaferio A., 2008, Space Sci. Rev., 134, 311
Donnert J., Dolag K., Lesch H., Müller E., 2009, MNRAS, 392, 1008
Einasto J., Klypin A. A., Saar E., Shandarin S. F., 1984, MNRAS, 206, 529
Einasto J. et al., 2011, A&A, 531, A75
Farnsworth D., Rudnick L., Brown S., Brunetti G., 2013, ApJ, 779, 189
Ferland G. J., Korista K. T., Verner D. A., Ferguson J. W., Kingdon J. B., Verner E. M., 1998, PASP, 110, 761
Finoguenov A., Briel U. G., Henry J. P., 2003, A&A, 410, 777
Fujishiro I., Maeda Y., Sato H., 1995, Proc. IEEE Visualization '95, Interval volume: A solid fitting technique for volumetric data display and analysis, pp. 151–158, CP–18
Geller M. J., Huchra J. P., 1989, Science, 246, 897
Giovannini G., Bonafede A., Feretti L., Govoni F., Murgia M., 2010, A&A, 511, L5
González R. E., Padilla N. D., 2010, MNRAS, 407, 1449
Gott J. R., III, Jurić M., Schlegel D., Hoyle F., Vogeley M., Tegmark M., Bahcall N., Brinkmann J., 2005, ApJ, 624, 463
Guo F., Oh S. P., 2008, MNRAS, 384, 251
Haardt F., Madau P., 1996, ApJ, 461, 20
Hahn O., Carollo C. M., Porciani C., Dekel A., 2007, MNRAS, 381, 41
Hallman E. J., O'Shea B. W., Burns J. O., Norman M. L., Harkness R., Wagner R., 2007, ApJ, 671, 27
Harrison C., Childs H., Gaither K. P., 2011, in Kuhlen T., Pajarola R., Zhou K., eds., Proc. EuroGraphics Symposium on Parallel Graphics and Visualization Eurographics Association, p. 131
Iapichino L., Schmidt W., Niemeyer J. C., Merklein J., 2011, MNRAS, 414, 2297
Kang H., Jones T. W., 2007, Astropart. Phys., 28, 232
Kang H., Ryu D., 2013, ApJ, 764, 95
Kang H., Ryu D., Cen R., Ostriker J. P., 2007, ApJ, 669, 729
Klar J. S., Mücket J. P., 2012, MNRAS, 423, 304
Komatsu E. et al., 2011, ApJS, 192, 18
Kronberg P. P., Kothes R., Salter C. J., Perillat P., 2007, ApJ, 659, 267
Maio U., Khochfar S., Johnson J. L., Ciardi B., 2011, MNRAS, 414, 1145
McCarthy I. G. et al., 2010, MNRAS, 406, 822
Meredith J. S., 2004, in Nuclear Explosives Code Developers Conference (NECDC), Lawrence Livermore National Laboratory, Livermore, CA
Meredith J. S., Childs H., 2010, in Proc. 12th Eurographics/IEEE - VGTC Conference on Visualization, EuroVis'10, Eurographics Association, Aire-la-Ville, Switzerland, p. 1241
Miniati F., Ryu D., Kang H., Jones T. W., Cen R., Ostriker J. P., 2000, ApJ, 542, 608
Nandra K. et al., 2013, preprint (arXiv:1306.2307)
Nicastro F., Krongold Y., Fields D., Conciatore M. L., Zappacosta L., Elvis M., Mathur S., Papadakis I., 2010, ApJ, 715, 854
Nicastro F. et al., 2013, ApJ, 769, 90
Ochsenbein F., Bauer P., Marcout J., 2000, A&AS, 143, 23
Obreschkow D., Power C., Bruderer M., Bonvin C., 2013, ApJ, 762, 115
Pfrommer C., Springel V., Enßlin T. A., Jubelgas M., 2006, MNRAS, 367, 113
Planck Collaboration VIII et al., 2013, A&A, 550, A134
Roncarelli M., Moscardini L., Tozzi P., Borgani S., Cheng L. M., Diaferio A., Dolag K., Murante G., 2006, MNRAS, 368, 74
Roncarelli M., Cappelluti N., Borgani S., Branchini E., Moscardini L., 2012, MNRAS, 424, 1012
Rudd D. H., Nagai D., 2009, ApJ, 701, L16
Ryu D., Kang H., Hallman E., Jones T. W., 2003, ApJ, 593, 599
Ryu D., Kang H., Cho J., Das S., 2008a, Science, 320, 909
Ryu D., Kang H., Cho J., Das S., 2008b, Science, 320, 909
Skillman S. W., O'Shea B. W., Hallman E. J., Burns J. O., Norman M. L., 2008, ApJ, 689, 1063

[4] http://www.cscs.ch

Smith R. K., Brickhouse N. S., Liedahl D. A., Raymond J. C., 2001, ApJ, 556, L91
Smith B. D., Hallman E. J., Shull J. M., O'Shea B. W., 2011, ApJ, 731, 6
Sousbie T., Pichon C., Colombi S., Novikov D., Pogosyan D., 2008, MNRAS, 383, 1655
Stoica R. S., Martínez V. J., Mateu J., Saar E., 2005, A&A, 434, 423
Tegmark M. et al., 2004, ApJ, 606, 702
Urban O. et al., 2014, MNRAS, 437, 3939
Vazza F., Brunetti G., Gheller C., 2009, MNRAS, 395, 1333
Vazza F., Brunetti G., Gheller C., Brunino R., 2010, New Astron., 15, 695
Vazza F., Dolag K., Ryu D., Brunetti G., Gheller C., Kang H., Pfrommer C., 2011, MNRAS, 418, 960
Vazza F., Brüggen M., Gheller C., Brunetti G., 2012, MNRAS, 421, 3375
Vazza F., Brüggen M., Gheller C., 2013, MNRAS, 428, 2366
Vazza F., Gheller C., Brüggen M., 2014a, MNRAS, 439, 2662
Vazza F., Brüggen M., Gheller C., Wang P., 2014b, MNRAS, 445, 3706
Viel M., Branchini E., Cen R., Ostriker J. P., Matarrese S., Mazzotta P., Tully B., 2005, MNRAS, 360, 1110
Vogelsberger M. et al., 2014, Nature, 509, 177
Werner N., Finoguenov A., Kaastra J. S., Simionescu A., Dietrich J. P., Vink J., Böhringer H., 2008, A&A, 482, L29
Zeldovich I. B., Einasto J., Shandarin S. F., 1982, Nature, 300, 407

APPENDIX A: PARAMETERS AND PERFORMANCE ANALYSIS

A1 Parameters analysis

Our filament identification procedure is characterized by six parameters, the most relevant being the mass density threshold $a_{\rm fil}$. Its value has been set according to various qualitative and statistical indications, as described in Section 3.3. Although $a_{\rm fil} = 1$ has been set, alternative values in the range 0.5-2.0 are acceptable. In order to verify the influence of $a_{\rm fil}$ on the results, we have calculated for simulation 1-1_1024 the mass–volume relation obtained adopting $a_{\rm fil} = 0.5, 0.75, 1.0, 2.0$. Fig. A1 compares the distributions obtained for the different values of $a_{\rm fil}$, showing that the trends and the dispersions obtained for the different thresholds are similar, hence the obtained scaling relations are reliable. On the other hand, the mass of the largest objects increases with decreasing $a_{\rm fil}$, due to percolation at low thresholds, and the normalizations change. This indicates that the methodology is robust for comparative studies of different models or multiple realizations of the same model. Absolute estimates (as, for instance, the number of objects with a given mass) have to be taken with some care.

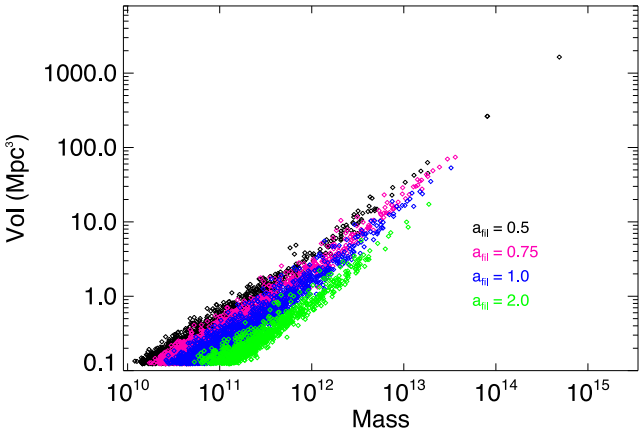

Figure A1. Mass–volume relation for simulation 1-1_1024 for different values of $a_{\rm fil}$.

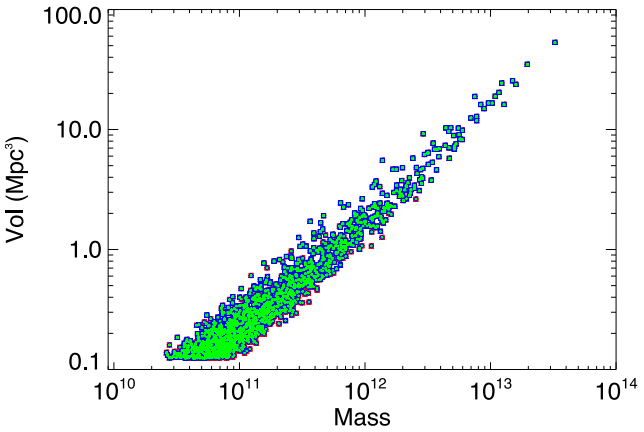

Figure A2. Mass–volume relation for simulation 1-1_1024 for $\alpha = 1.0$ (red), $\alpha = 2.0$ (blue), $\alpha = 4.0$ (green) and $L_\varphi = 0.1$ (crosses), $L_\varphi = 2.5$ (diamonds), $L_\varphi = 5.0$ (triangles), $L_\varphi = 10.0$ (squares). The overall influence of the different settings on the mass–volume statistics is shown.

The remaining five parameters are as follows.

(i) $a_{\rm cl}$: mass density threshold to select the highest peaks of the mass distribution;
(ii) β: scale factor to get clusters' radii of the order of 1 Mpc;
(iii) $V_{\rm res}$: objects whose volume is below this value are discarded;
(iv) α: maximum ratio between the axes of the bounding box containing a filament;
(v) φ: filling factor; filaments whose volume is larger than ϕ times the associated bounding box volume, are discarded.

The first three parameters can be considered as fixed, being related to the physical properties of galaxy clusters (the first two) and to the spatial resolution of the simulations (the third). For the remaining two parameters, we have performed the identification procedure several times, changing their values in order to investigate the influence on the results. Again, we have used simulation 1-1_1024 as a representative case.

Fig. A2 shows the mass–volume relation for all 12 cases obtained setting $\alpha = 1, 2, 4$ and $L_\varphi = 0.1, 2.5, 5, 10$, this last parameter being the ratio between the bounding box diagonal length and the radius of the inscribed cylinder (see Section 3.3 for more details): the larger the value of L_φ, the smaller the threshold filling factor. Fig. A3 shows a subset of the mass–volume data, obtained selecting only those values obtained for $L_\varphi = 5$ and $\alpha = 2$, respectively (the values adopted in this work). Figs A4 and A5 show the mass–temperature relation for the same parameter settings.

It is clear how changing the value of these two parameters has a minor impact on the results, all the main characteristics of the presented statistics being preserved. However, a proper selection of their values allows eliminating outliers and objects whose geometry is not compatible with that expected for typical filaments (e.g. small, round shaped clumps), fine tuning the results. The values $L_\varphi = 5$ and $\alpha = 2$ have proved to be effective without being too restrictive, leading to the loss of significant objects.

A2 Performance analysis

The data analysis has been performed on the PILATUS[5] HPC data processing system of ETHZ-CSCS, using the client-server

[5] http://user.cscs.ch/computing_resources/pilatus

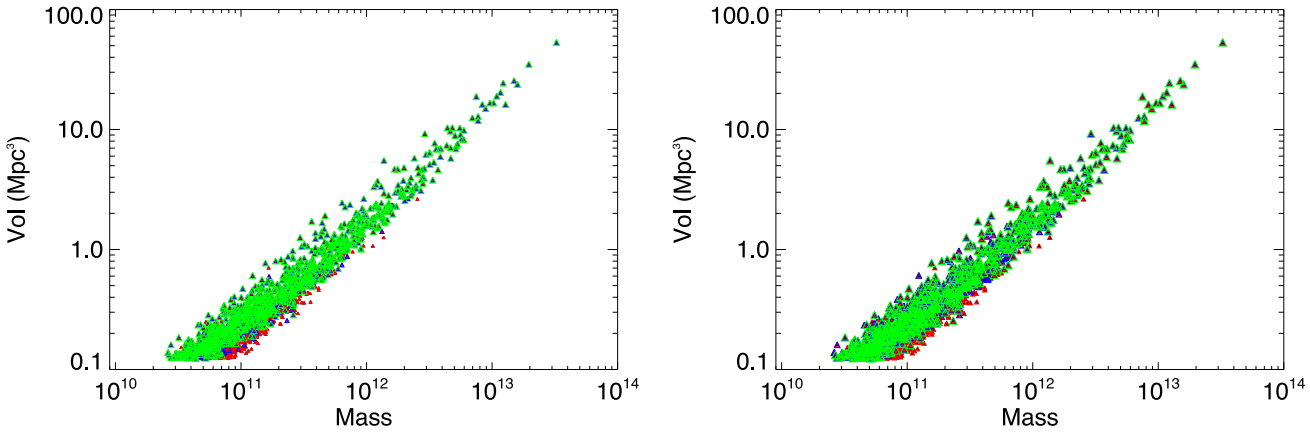

Figure A3. Mass–volume relation for simulation 1-1_1024 for $\alpha = 1.0$ (red), $\alpha = 2.0$ (blue), $\alpha = 4.0$ (green) and $L_\varphi = 5.0$ (left panel) and $L_\varphi = 0.1$ (black), $L_\varphi = 2.5$ (red), $L_\varphi = 5.0$ (blue), $L_\varphi = 10.0$ (green) and $\alpha = 2.0$ (right panel). The impact of the various settings for each of the two parameters individually on the mass–volume statistics is shown.

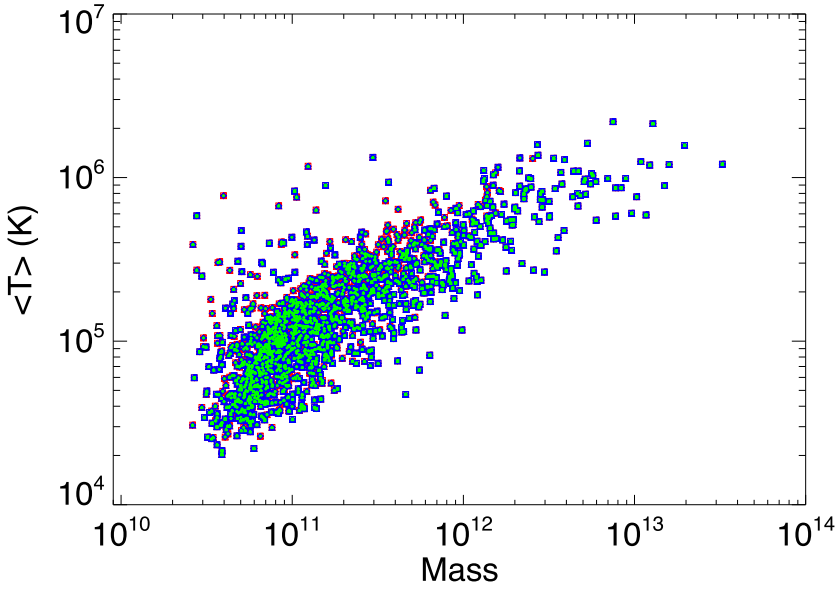

Figure A4. Mass–temperature relation for simulation 1-1_1024 for $\alpha = 1.0$ (red), $\alpha = 2.0$ (blue), $\alpha = 4.0$ (green) and $L_\varphi = 0.1$ (crosses), $L_\varphi = 2.5$ (diamonds), $L_\varphi = 5.0$ (triangles), $L_\varphi = 10.0$ (squares). The overall influence of the different settings on the mass–temperature statistics is shown.

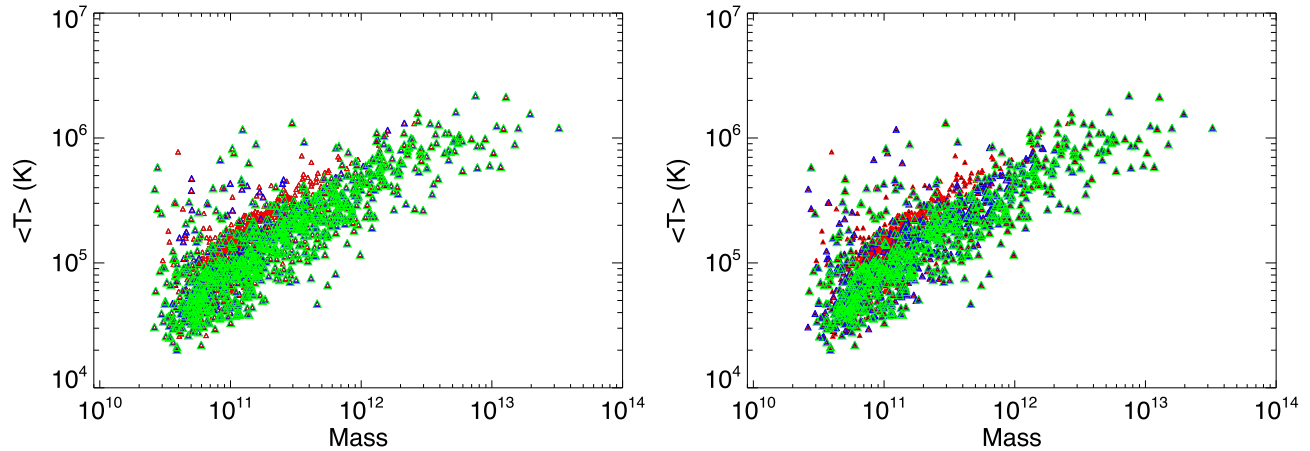

Figure A5. Mass–temperature relation for simulation 1-1_1024 for $\alpha = 1.0$ (red), $\alpha = 2.0$ (blue), $\alpha = 4.0$ (green) and $L_\varphi = 5.0$ (left panel) and $L_\varphi = 0.1$ (black), $L_\varphi = 2.5$ (red), $L_\varphi = 5.0$ (blue), $L_\varphi = 10.0$ (green) and $\alpha = 2.0$ (right panel). The impact of the various settings for each of the two parameters individually on the mass–temperature statistics is shown.

Table A1. Strong scalability for the 2-1_1024 model. Computing time (Column 2) and memory usage (Column 3) are shown as a function of the number of cores (Column 1).

MPI tasks	CPU time (s)	Memory (GB)
1	633	17.309
2	369	18.381
4	207	19.296
8	123	21.229
16	83	25.256
32	63	34.592
64	50	53.158

Table A2. Computing time (Column 2) and memory usage (Column 3) for selected models using 32 cores.

Model	CPU time (s)	Memory (GB)
3-1_512	20	18.166
3-1_1024	52	32.526
2-1_1024	63	34.592
1-1_1024	67	36.785
1-1_2048	771	185.541

2.8 MPI-parallel version of VisIt. Pilatus is a cluster composed of 44 nodes each with 2 Intel Xeon CPUs E5-2670 (2.60GHz, 16 cores, 64GB RAM).

In a first series of tests, strong scalability (i.e. the change in computing time with increasing number of MPI tasks) is investigated. The 2-1_1024 model is adopted as reference. Table A1 presents the CPU time as a function of the number of MPI tasks. Acceptable scalability (though not linear) is achieved up to 16 tasks, although at 32 and 64 tasks the computing time is still decreasing. In the same table, the memory usage is shown. Due to the data replica needed for parallel processing, the memory required grows with the number of tasks, reaching, at 64 tasks, more than three times that required for a single task, which is about 17GB. Two variables, mass density and temperature, are used each represented by a 1024^3 cells floating point single precision variable, accounting for 8 GB. The remaining 50 per cent of memory is required to handle isosurfaces and connected components.

For the entire data analysis, we have set the number of MPI tasks to 32. This represents a good trade-off between computing time and memory usage. In Table A2 we present the CPU time needed to run the filament reconstruction procedure for the different simulations. Only the 1-1_2048 case required 64 MPI tasks, due to memory constraints. The '0', 'c1' and 'c2' models have similar requirements.

Table A3. Minimum (Column 2) and maximum (Column 3) memory usage on the different MPI tasks for the 2-1_1024 model as a function of the number of cores (Column 1)

MPI tasks	Min Mem (GB)	Max Mem (GB)
4	4.553	5.140
8	2.586	2.817
16	1.443	1.703
32	1.011	1.151
64	0.770	0.868

The usage of 32 tasks keeps the CPU time reasonably low. This is particularly important during the set-up of the different model parameters when the filament identification procedure must be repeated many times, with slightly different values of each parameter. Note that the analysis of the 1-1_2048 case requires a huge memory allocation (more than 185 GB). Furthermore, in the 1024^3 models, the memory usage grows from 3-1_512 to 1-1_2048 runs because of the increasing simulation volume and hence the larger number of identified objects.

Finally, we analysed the load balancing among MPI tasks, to check if the workload is evenly distributed among the cores. Again, we adopt as reference the 2-1_1024 model. As a measure of the load balancing, in Table A3 we show the minimum and maximum memory used by the various tasks. This can be assumed as an effective measure for the workload, due to the homogeneous spatial distribution of the filaments. In all tests, the difference between the maximum and minimum values, so the work imbalance, is between the 11 and 15 per cent.

The results of the performance analysis clearly show the feasibility of this approach for big data sets by exploiting HPC systems and parallel processing, and its potential scalability to the analysis of future larger simulations.

This paper has been typeset from a TEX/LATEX file prepared by the author.